CHIMIE NOUVELLE

LA REVUE DE CONTACT DE LA **SOCIÉTÉ ROYALE DE CHIMIE**

38ème année - **mars 2020**

CN **133**

Sommaire

Parution : trimestrielle

Avec le soutien du Fonds National de la Recherche Scientifique.
Les articles paraissant dans Chimie nouvelle sont repris dans CHEMICAL ABSTRACTS

Editeur responsable : Claudine Buess-Herman,
ULB, CP 160/07,
avenue Roosevelt 50, 1050 Bruxelles

Les articles sont soumis à un processus de reviewing.
Les annonces publicitaires sont établies sous la responsabilité des firmes.

« CHIMIE NOUVELLE » est un titre déposé

ISBN 0771-730X

Simon COTTON
School of Chemistry, University of Birmingham, Edgbaston, Birmingham B15 2TT, United Kingdom - s.cotton@bham.ac.uk

Two centuries of the rare earths

Abstract
The rare earths are important in the history of the Periodic Table, not least because no one knew how many there were. Their separation was also a challenge, owing to the similarity of properties of neighbouring elements, a manifestation of the lanthanide contraction. After initial uncertainty, it was realised that these elements exhibited predominantly the +3 oxidation state, but over the past century compounds of a few elements in the +2 state have been synthesised, and with recent breakthroughs all lanthanides have been forced into the +2 state, with the right choice of ligand. Certain elements, notably cerium, exhibit the +4 oxidation state in their chemistry. Studying the structures of compounds of the elements has been very rewarding, with a wide range of coordination numbers from 2 to 12. Among these compounds, diketonate complexes have had many applications, from lanthanide shift reagents to organic light-emitting diodes.
Applications bring lanthanides into all homes, whether with batteries, lighting, computer hard drives, fibre optics or wind turbines. Since the discovery of yttrium, the first rare earth, over two centuries have passed; now, with the latest discovery that lanthanides have a role in enzymes, we can say that these elements have come into their own.

Keywords
Rare earth; lanthanides; Periodic Table.

Back in 2017, the United Nations designated 2019 as the International Year of the Periodic Table of the Chemical Elements. Dmitri Mendeleev first presented his periodic table in 1869. The elements were arranged according to their atomic mass, with certain additional modifications which distinguished it from previous tables. For instance, some gaps were left blank for elements that remained to be discovered (e.g., Sc, Ge, Ga).

1. Discovery

The first five rare earth elements were known when Mendeleev proposed his first periodic table, starting with Carl Axel Arrhenius's discovery of a black stone at a mine near Ytterby in 1787, consequently named ytterbite. In 1794 Johan Gadolin went further with the isolation of the oxide of a new element which he named yttrium. Later on, this small village gave its name to other three elements, namely erbium, terbium, and ytterbium. Together with the much lighter scandium, yttrium and the lanthanides are often referred to collectively as the rare earths. This is a double misnomer, as 'earths' are strictly the oxides of elements, and they are certainly not rare (Figure 1). Although not as abundant as lighter elements, they are more common than well-known elements such as platinum metals, mercury, silver, and gold. Yttrium is considered as a lanthanide element due to its similarities, in both atomic size and chemistry, with heavier

lanthanides, most notably holmium. The reduced size and mass of scandium involve important differences in its chemistry. High-abundance ores containing a specific rare earth element are missing, and therefore, the separation of mixtures of similar elements into distinct species is an important part of the extraction process.

The term 'lanthanide' derives from the similarity of this series of elements to the first member, lanthanum, which itself gets its name from the Greek word *lanqanei*ν (*lanthanein*), 'to be hidden', as it was first discovered as an impurity in cerium.

2. Rare earth ores

Looking first at their overall global abundance, within the lanthanide series the lighter lanthanides are more abundant than the heavier ones; secondly, that the elements with even atomic number are more abundant than those with odd atomic number.

Among the principal ores, bastnasite, $LnFCO_3$, and monazite, $(Ln,Th)PO_4$, are both richer in earlier lanthanides, espcially La and Ce; in contrast, xenotime $(Y, La)PO_4$, is richer in later lanthanides (e.g. Gd-Lu) and strikingly more so in yttrium. The other very important source of these elements is a type only found in southern China, the 'ion-absorption ores'. These are formed by slow weathering of lanthanide-containing igneous rocks (e.g. granite) then the Ln^{3+} ions are adsorbed by kaolinic clays. These ores have a low abundance of rare earths (ca. 0.1%) but are very abundant and are also easy to mine. Their composition varies from place to place; they generally contain significant amounts of the middle lanthanides (e.g. Gd to Er) and also yttrium, but sometimes the lanthanum content is significant. Although their content of heavy lanthanides like holmium, thulium and lutetium is low, these ores have become the main source of the heavier lanthanides in particular because of the sheer scale of these deposits, [1, 2].

At the time that Mendeleev created his first Periodic Table, only five of the rare earths were known – yttrium, lanthanum, cerium, erbium and terbium. It was not until the later part of the 19th century that improved separation techniques, along with spectroscopic analysis, allowed the

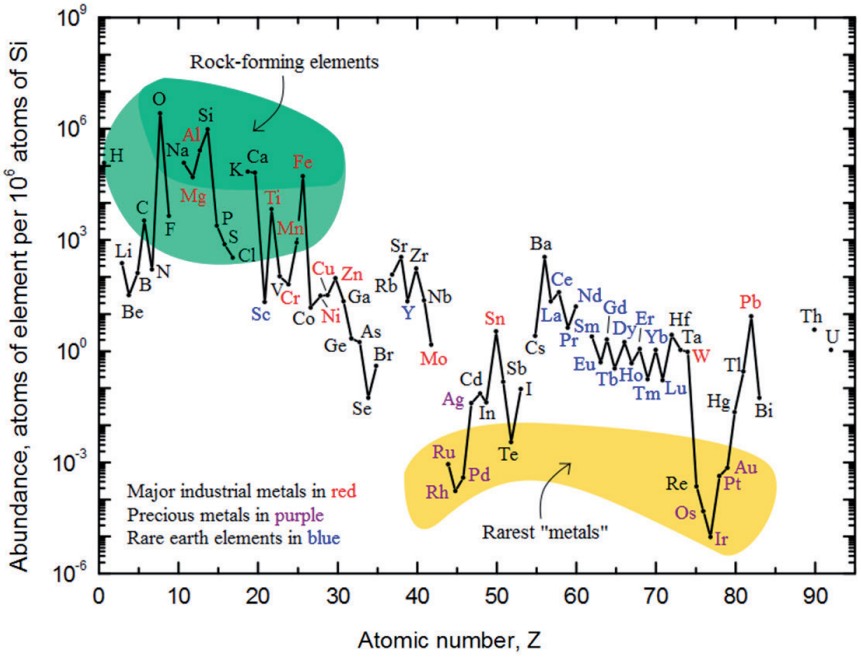

Figure 1. Abundances of the chemical elements.
Source: http://upload.wikimedia.org/wikipedia/commons/0/09/Elemental_abundances.svg
[from WikiCommons]

discovery and isolation of all but one of the elements by 1907 (Lutetium).

Initially, Mendeleev faced some problems in positioning these elements [3], as he assumed that like many metals they typically had oxidation states of +2 in their compounds, leading to incorrect atomic masses (Fig. 2).

Ueber die Beziehungen der Eigenschaften zu den Atomgewichten der Elemente. Von D. Mendelejeff. — Ordnet man Elemente nach zunehmenden Atomgewichten in verticale Reihen so, dass die Horizontalreihen analoge Elemente enthalten, wieder nach zunehmendem Atomgewicht geordnet, so erhält man folgende Zusammenstellung, aus der sich einige allgemeinere Folgerungen ableiten lassen.

			Ti = 50	Zr = 90	? = 180
			V = 51	Nb = 94	Ta = 182
			Cr = 52	Mo = 96	W = 186
			Mn = 55	Rh = 104,4	Pt = 197,4
			Fe = 56	Ru = 104,4	Ir = 198
			Ni = Co = 59	Pd = 106,6	Os = 199
H = 1			Cu = 63,4	Ag = 108	Hg = 200
	Be = 9,4	Mg = 24	Zn = 65,2	Cd = 112	
	B = 11	Al = 27,4	? = 68	Ur = 116	Au = 197?
	C = 12	Si = 28	? = 70	Sn = 118	
	N = 14	P = 31	As = 75	Sb = 122	Bi = 210?
	O = 16	S = 32	Se = 79,4	Te = 128?	
	F = 19	Cl = 35,5	Br = 80	J = 127	
Li = 7	Na = 23	K = 39	Rb = 85,4	Cs = 133	Tl = 204
		Ca = 40	Sr = 87,6	Ba = 137	Pb = 207
		? = 45	Ce = 92		
		?Er = 56	La = 94		
		?Yt = 60	?Di = 95		
		?In = 75,6	Th = 118?		

1. Die nach der Grösse des Atomgewichts geordneten Elemente zeigen eine stufenweise Abänderung in den Eigenschaften.
2. Chemisch-analoge Elemente haben entweder übereinstimmende Atomgewichte (Pt, Ir, Os), oder letztere nehmen gleichviel zu (K, Rb, Cs).
3. Das Anordnen nach den Atomgewichten entspricht der *Werthigkeit* der Elemente und bis zu einem gewissen Grade der Verschiedenheit im chemischen Verhalten, z. B. Li, Be, B, C, N, O, F.
4. Die in der Natur verbreitetsten Elemente haben *kleine* Atomgewichte

Figure 2. Mendeleev's paper (1869) entitled "On the Relationship of the Properties of the Elements to their Atomic Weights".

'One orders the elements according to increasing atomic weight in vertical rows so that the horizontal rows contain analogous elements, still ordered by increasing atomic weight, one obtains the following arrangement, from which a few general conclusions may be derived.'

In points 1-3 he says: - 1. If arranged according to their atomic weights, the elements show an evident gradual variation of properties. 2. Chemically analogous elements have either similar atomic weights (Pt, Ir, Os), or weights which increase by equal increments (K, Rb, Cs). 3. The arrangement according to atomic weight corresponds to the *valency* of the element and to a certain extent the difference in chemical behaviour, for example Li, Be, B, C, N, O, F. He lists (in order of increasing mass) erbium, yttrium, cerium, lanthanum and didymium. Note that Di refers to 'didymium', the mixture of Pr, Nd and Sm which was at that time considered to be an element. Yt was then the symbol for yttrium; a space has been left for an element of atomic mass 45, now known to be scandium. D. Mendeleev, *Zeitschrift für Chemie*, 1869, **12**, 405-406 and https://web.lemoyne.edu/giunta/EA/MENDELEEVann.HTML

By 1871 he had changed his ideas [4], taking the formulae of the oxides to be M_2O_3, leading to atomic masses in line with today's values, though he appeared to believe that lanthanum had an oxidation state of (+4).

Whilst in the latter part of the 19th century new lanthanides were rapidly being discovered, no one knew how many there were until H. G. J. Moseley (1887-1915) and his study of X-ray spectra of the elements introduced the concept of atomic number. Moseley's Law showed that the square root of the frequency of the emitted X-ray is proportional to the atomic number, and revealed that the only rare earth remaining to be discovered was element 61. [5]

Several claims for this element were made by researchers, notably in 1926 when "Illinium" and "Florentium" were simultaneously reported by American and Italian researchers. [6] None of these claims could be supported by other researchers. Lines in spectra claimed to be from element 61 were found to be due to other elements, present as impurities.

It was realised that Element 61 would be radioactive and too short-lived to be found on earth, and it was finally recognised in 1946 among the fission products of uranium. [7]

3. Oxidation states and separating the elements

All the lanthanides form stable Ln^{3+} ions in aqueous solution, and since there is very little significant aqueous chemistry in other states, this affects separating and purifying the individual elements. Neighbouring elements have very similarly sized ions, so that their compounds have similar solubilities. Initially, however, fractional crystallisation, which takes advantage of small differences in solubility of compounds of neighbouring metals, was employed, though multiple stages were necessary, most famously in the case of thulium, where 15 000 operations were necessary to remove the last traces of erbium.[8]

Lanthanides are prominent among the fission products of uranium, so that during the Manhattan project new separation methods were developed, notably cation-exchange chromatography, where the elements are eluted from ion-exchange resins. Initially complexing agents like citrate or α-hydroxy-isobutyrate were employed, but subsequently the complexes of EDTA (Ethylenediaminetetraacetate) were found to have much higher stability constants. [9]

Such separations work very well on the small scale to produce high-purity samples of individual lanthanides, but on the industrial scale solvent extraction is the preferred technique. Typically, an aqueous solution of the mixed lanthanides is extracted using a complexing agent like tributyl phosphate (TBP) or di-2-ethylhexyl phosphoric acid (HDEHP) in kerosene, complexes such as $[Ln(NO_3)_3(TBP)_3]$ becoming more stable and more soluble in kerosene with increasing atomic number. Counter-current methods are employed to provide a multistage process that gives enhanced separations. [10]

4. The lanthanide contraction

These separations work because of the lanthanide contraction (a term coined in 1925 by the Norwegian mineralogist Victor Goldschmidt), the decreasing size of the lanthanide atoms and ions with increasing atomic number [11]. This accounts for subtle and progressive changes often observed in properties of lanthanide compounds, though the ionic radii are the most obvious manifestation. This impinges on bond lengths in lanthanide compounds, so that in a series of isostructural compounds with the same coordination number, the lanthanide – bond length decreases steadily with increasing atomic number.

Thus for the family $[Ln(terpy)(NO_3)_3(H_2O)_n]$ (terpy = 2,2';6',2"-terpyridine) the trends in the Ln-N, Ln-O and Ln-OH_2 are illustrated in Fig. 3. There is a smooth variation with increasing atomic number (and decreasing ionic radius) of the lanthanide, with discontinuities at the point of coordination number change. Thus there is a gradual decrease in bond length with increasing Z for the 10 coordinate series $[Ln(terpy)(NO_3)_3(H_2O)]$ (Ln = Ce-Ho), but there

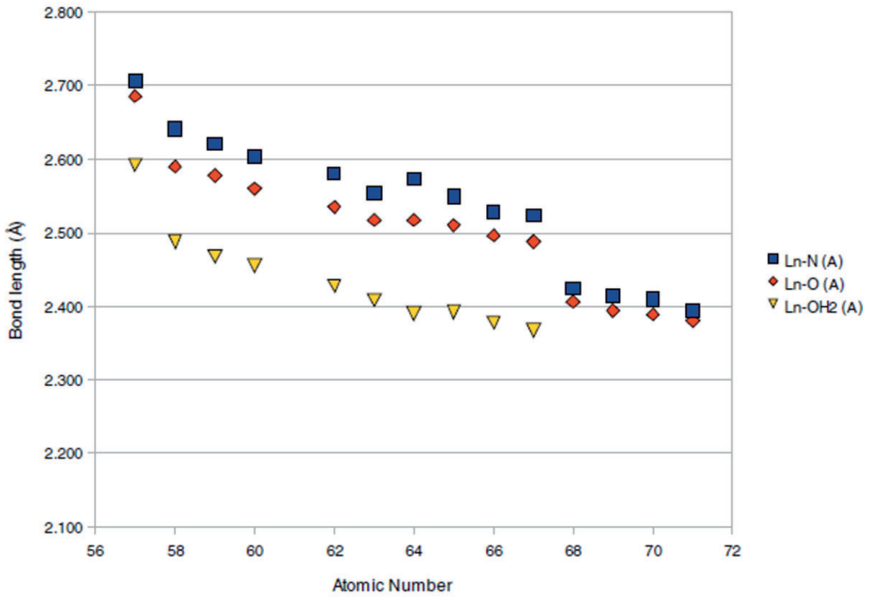

Figure 3. Bond lengths in the family $[Ln(terpy)(NO_3)_3(H_2O)_n]$.
(with permission from S. A. Cotton and P. R. Raithby, *Co-ordination Chem. Revs.*, 2017, **340**, 220-231)

is a sharp step up to the 11 coordinate [La(terpy)$(NO_3)_3(H_2O)$] at one end, and the 9 coordinate [Er(terpy)$(NO_3)_3$] at the other [12].

5. Coordination numbers in lanthanide compounds

The propensity of many transition metal ions, notably Co^{3+}, to indulge predominantly in forming six coordinate, octahedral compounds was a cornerstone of Alfred Werner's coordination theory [13]. Chemists tended to assume that the lanthanides behaved similarly. It took some time for X-ray diffraction to be applied to lanthanide complexes, so that it was not until the late 1930s that structures were reported of the hydrated ethylsulfates $[Ln(H_2O)_9]$ $(EtSO_4)_3$ (Ln = Y, La, Ce, Pr, Nd, Sm, Gd, Dy) (Ketelaar, 1937) and hydrated neodymium bromate, $[Nd(H_2O)_9]$ $(BrO_3)_3$, in 1939 (Helmholz 1939), which revealed tricapped trigonal prismatic nine coordination. Despite that, the view that lanthanides adopted six coordination persisted into the 1960s.

The report of 12-coordinate $[Ce(NO_3)_6]^{3-}$ ions in $Ce_2Mg_3(NO_3)_{12}$. $24H_2O$ [15] was followed by the realisation that the familiar complexing agent EDTA was not big enough to totally encapsulate Ln^{3+} ions, leaving space for water molecules enter the coordination sphere, with Lynn Hoard's group discovering nine-coordinate $[La(EDTA)(OH_2)_3]^-$ ions in K La(EDTA). $8H_2O$. Not only can heavier lanthanides can form eight coordinate ions such as $[Er(EDTA)(OH_2)_2]^-$, but sometimes the counter-ion can affect which complex ion crystallises, with nine coordination in Na $[Er(EDTA)(H_2O)_3].5H_2O$ and eight coordination in NH_4 $[Er(EDTA)(OH_2)_2]^-$ and $[C(NH_2)_3]_2[Er(EDTA)(H_2O)_2]ClO_4.6H_2O$ [17]. Likewise, whilst the ethylsulfate, bromate and triflate salts of the hydrated lanthanide ions all contain 9 coordinate $[Ln(H_2O)_9]^{3+}$ ions [18] the perchlorates have octahedral $[Ln(H_2O)_6]^{3+}$ ions [19]. The most normal coordination number for the lanthanide ions is 8 or 9 [20].

Research from the late 1960s in the laboratory of D. C. Bradley at Queen Mary College London led to the isolation of $[M\{N(SiMe_3)_2)_3]$ (M = Sc, Ti, V, Cr, Fe) with the unprecedented coordination number for these metals of three, enforced by the very bulky bis(trimethylsilyl)amide ligand [21]. A natural extension of this was to use this ligand to attempt the synthesis of similar lanthanide compounds, success being achieved in the three-coordinate $[Ln\{N(SiMe_3)_2)_3]$ (Ln = Y, La, Ce, Pr, Nd, Sm, Eu, Gd, Ho, Yb, and Lu), making these the first compounds of these metals with this coordination number [22]. Unlike the d-block analogues, the coordination geometry here is trigonal pyramidal, a distortion ascribed to the presence of β-Si–C agostic interactions, a view supported by density functional theory (DFT) calculations [23]. Very bulky ligands were also employed in the synthesis of the first four coordinate compounds, $[Li(thf)_4]$ [Ln(2,6-dimethylphenyl)$_4$] (Ln = Yb, Lu) [24], and in the two coordinate $[Yb\{C(SiMe_3)_3\}_2]$ [25].

6. β-diketonate complexes and their applications.

Lanthanide β-diketonates were among the first lanthanide complexes to be reported; syntheses including $[La(acac)_3(H_2O)_2]$ and $[Ce(acac)_4]$ (Hacac = acetylacetone or pentane-2,4-dione), were published by Georges Urbain in 1897 [26] and many others have followed. The diketonate ligands ($R_1COCHCOR_2^-$) afford a wide range of easily synthesised lanthanide complexes, which have found numerous applications discussed below.

Unlike the familiar octahedrally coordinated $[M(acac)_3]$ (M = Sc-Co), the lanthanides expand their coordination sphere by adduct formation with Lewis bases (unless the diketonate has very bulky substituents). Thus $[Ln(acac)_3(H_2O)_2]$ (Ln = La-Ho, Y) are eight coordinate and $[Yb(acac)_3(H_2O)_2]$ is seven coordinate – only a few complexes with very bulky substituents, such as $[Lu(tmhd)_3]$ (Htmhd = 2,2,6,6-tetramethyl-3,5-heptanedione (also known as Hdpm)),
have sic coordination, and even these tend to accept additional donors. In contrast, $[Ho(hfac)_3(bipy)_2]$ (Hhfac = hexafluoroacetylacetone, 1,1,1,5,5,5-hexafluoro-2,4-pentanedione; bipy = 2,2'bipyridyl)

has ten coordinate holmium [27]. Some complexes like $[Ln(tmhd)_3]$ and $[Ln(tmhd)_3]_2$](Ln = Tb-Ho) and adopt monomeric six coordinate or dimeric seven coordinate structures depending upon crystal growth conditions [28].

The volatility of many β-diketonate complexes makes them suitable for a number of applications, including precursors for metal-organic chemical vapour deposition (MOCVD) and atomic layer deposition (ALD) [27]. Compounds like $[Ln\{tmhd\}_3]$ have both advantages and disadvantages in comparison with alternative precursors, such as $[Ln\{(CpR\}_3]$ (R e.g. Me, Et, ^{i} Pr), alkoxides and |$[Ln(N(SiMe_3)_2)_3]$ [27, 29]. Thus their lower reactivity and ease of synthesis makes the diketonate complexes easier to make and handle than the cyclopentadienyls or the bis(trimethylsilyl)amides, but the diketonates are harder to activate and require higher growth temperatures. Their propensity for adduct formation has been useful in several aspects of the chemistry of these complexes. From 1969 [30], paramagnetic complexes such as $[Ln(tmhd)_3]$ (Ln = Eu, Pr) and $[Eu(fod)_3]$ (Hfod = 6,6,7,7,8,8,8-heptafluoro-2,2-dimethyl-3,5-octanedione) enjoyed considerable success as NMR shift reagents (probably the first time that many organic chemists encountered lanthanides), which simplified ^{1}H NMR spectra of organic compounds by reducing overlap of signals and giving well resolved spectra [31]. This relied on the molecule being studied (e.g. an alcohol) forming an adduct with $[Ln(diketonate)_3]$. Within two decades, the coming of high-frequency NMR spectrometers rendered common applications of lanthanide shift reagents redundant, though niche applications remain, like chiral lanthanide shift reagents. $[Ln(fod)_3]$ complexes are also used as Lewis acid catalysts in organic reactions, such as Diels-Alder syntheses [27].

7. Properties and applications of lanthanide-based compounds

Electronic spectra

With the exception of La^{3+} and Lu^{3+}, the Ln^{3+} (Ln = lanthanide) ions have a partly filled 4f subshell. They absorb electromagnetic radiation, exciting the ion from its electronic ground state to a higher excited state. Because the 4f orbitals are well shielded by outer (5s, 5p) filled subshells, they play little part in bonding and are little influenced by surrounding ligands. Consequently, the transitions in their absorption spectra are typically sharp and line-like, in contrast to d-d transitions in spectra of transition metals ions [32, 33]. A few ions, such as Nd^{3+}, have spectra containing certain "hypersensitive" transitions, absorptions whose intensity and structure varies with their environment (though much less than observed with d block ions) [34].

Lasers

Lasers rely on stimulated emission of light. The most popular rare earth lasers are rods made of yttrium aluminium garnet (YAG; $Y_3Al_5O_{12}$) containing Nd^{3+} ions. They are fitted with mirrors at each end, one a partly reflecting mirror. A lamp is used to 'pump' the system so that an excess of the neodymium ions are in an excited state (e.g. $^4F_{5/2}$ or $^4F_{7/2}$); this means that more ions can emit electrons than absorb. These excited ions undergo a non-radiative decay to the long-lived $^4F_{3/2}$ excited state, creating a 'population inversion', where an excess of the Nd^{3+} ions are in this state. The $^4F_{3/2}$ state can relax to the $^4I_{11/2}$ state radiatively, emitting a photon. This emission process can be triggered by an incident photon of appropriate energy, 'stimulated emission'. The emitted photons can be reflected backwards and forwards in the rod, stimulating the release of more and more photons. Eventually there is such a large build-up of photons that they emerge from the rod as an intense beam of coherent monochromatic light, the laser beam [35].

Luminescence

Many Ln^{3+} ions are important for their luminescence under UV irradiation. The most important emitters of visible light are Eu^{3+} (red) and Tb^{3+} (green), whilst several, such as Yb^{3+}, Nd^{3+} and Er^{3+}, luminesce in the near-IR. Red emission from Eu^{3+}, in Y_2O_3, was first noted in 1906 by Georges Urbain [36], and in 1942, Weissman rec-

ognized that coordinating organic ligands, including β-diketonates, absorbed strongly and that this could be transferred to a Eu^{3+} ion for subsequent emission, which is the "antenna effect" [37]. Initial excitation of the ligand to its first excited singlet state can be followed successively by intersystem crossing to the triplet state, followed by another non radiative transition to an excited state of the europium ion, which can emit back to its ground state by photoluminescence. This can be applied to other lanthanides, of course. $[Eu(TTA)_3(phen)]$ (Htta = 2-thenoyltrifluoroacetone, 4,4,4-trifluoro-1-(2-thienyl)-1,3-butanedione; phen = 1,10-phenanthroline) (Fig. 4) is one of the brightest red emitters known; widely used as a red emitter in OLEDs (organic light-emitting diodes) [38].

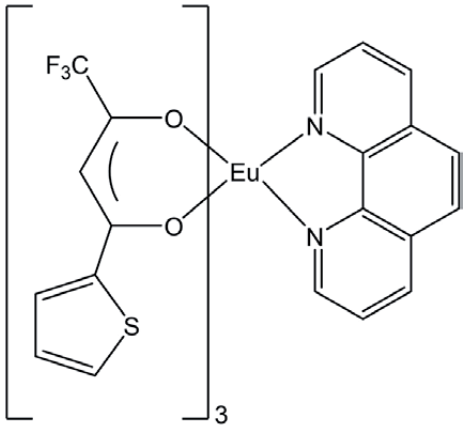

Figure 4. The complex $[Eu(TTA)_3(phen)]$, important in red-emitting devices.

One application of the antenna effect was conceived in the wake of the terrorist attacks in New York on September 11th 2001, when envelopes containing anthrax spores (*Bacillus anthracis*) were delivered to two USA Senators and to several media outlets; five people were killed. Anthrax spores contain around 10% by mass of calcium dipicolinate (DPA^{2-}), which acts as a biomarker. The Tb^{3+} aqua ion is only weakly luminescent because of vibronic coupling between O-H groups in the coordinated water molecules with the excited Tb^{3+} ion, which provides a nonradiative decay pathway. Adding DPA^{2-} to Tb^{3+} ions produces an enhancement of luminescence by three orders of magnitude, as dipicolinate acts as an antenna, whose lowest triplet state matches the lowest emitting level of the Tb^{3+} ion. The effect can be enhanced further, by additionally including the hexadentate macrocylic ligand $DO2A^{2-}$ (DO2A = 1,4,7,10-tetraazacyclododecane-1,7-diacetate); the resulting nine coordinate complex (Fig. 5) has no deactivating waters in the coordination sphere and has even higher emission [39].

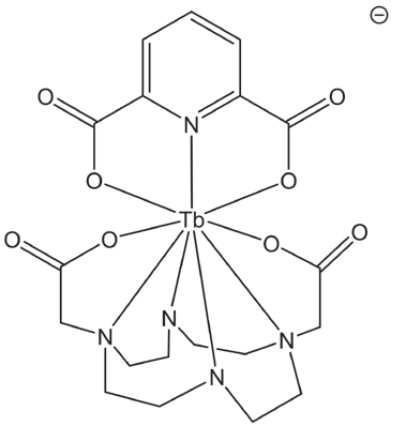

Figure 5. The structure of the $[Tb(DO2A)(DPA)]^-$ complex ($DO2A^{2-}$ = 1,4,7,10-tetraazacyclododecane-1,7-diacetate; DPA^{2-} = dipicolinate)

Lanthanides are especially important because of their lighting and display applications. This first became important when colour televisions became widespread from the 1960s, particularly the red emitters based in Eu(III), still used today. Following on from this, lanthanide phosphors were applied to fluorescent tubes; materials used have included red: Y_2O_2S or Y_2O_3: Eu^{3+}; green: $LaPO_4$: Ce^{3+}, Tb^{3+}, $CeMgAl_{11}O_{19}$:Tb^{3+} or Y_2O_2S: Tb^{3+}: blue: $BaMgAl_{10}O_{17}$:Eu^{II}. Uses have spread to compact fluorescent lamps, plasma TVs and computer monitors, successive generations of phosphor being chosen for greater energy efficiency [40].

Chemistry and oxidation states in lanthanide compounds

As already noted, when Mendeleev conceived his table, it was widely believed that rare earths like La, Ce and Y had oxidation states of +2 in their compounds, like most other metals. This meant that compounds of the elements were assigned the wrong formulae (e.g. MO), leading to incorrect atomic masses and problems with positioning them in the Periodic Table in 1869 [3]. By 1871, he had modified his ideas, recognising that the oxides were M_2O_3, and his values of the atomic

masses were in the correct region (e.g. Y 88, Ce 140, Er 178), though he seems to have thought that lanthanum was tetravalent, leading to an atomic mass of 180 [4]. Even though many lanthanide elements were not identified yet at that time, Mendeleev tried to accommodate the existing rare earths along with the other elements. It was eventually achieved in 1905 with Alfred Werner who positioned all lanthanides in a horizontal block of their own [41].

Until recent times, it was recognised that the chemistry of the lanthanides was largely that of the +3 oxidation state [42]. Cerium was known additionally to form compounds in the +4 state, most familiarly the well known oxidant $(NH_4)_2[Ce(NO_3)_6]$, widely used by organic chemists. As the 20th century proceeded, halides of certain divalent lanthanides were synthesised, usually by hydrogenic reduction of the trihalides, such as $SmCl_2$ (1906), followed by $EuCl_2$ (1911), YbI_2 (1929) and the other LnX_2 (X = F, Cl, Br, I; Ln = Sm, Eu, Yb) [43]. The Eu^{2+} aqua ion was found to be reasonably stable in the absence of oxygen, less so the corresponding ions of samarium and ytterbium. So for many years, the +2 oxidation state was associated with Sm^{2+} (f^6); Eu^{2+} (f^7) and Yb^{2+} (f^{14}), and the idea grew that these were stable because of the half-filled or filled 4f subshells. Subsequently it was found that the +2 state was accessible for other lanthanides by means of comproportionation reactions, high-temperature 'metallothermic reduction' affording further dihalides, notably $NdCl_2$, NdI_2, DyI_2 and TmI_2, with electron configurations away from the half-filled or filled sub-shell, Nd^{2+} (f^4); Dy^{2+} (f^{10}); Tm^{2+} (f^{13}) [44].

$$Nd + 2\ NdCl_3 \rightarrow 3\ NdCl_2$$
$$Tm + 2\ TmI_3 \rightarrow 3\ TmI_2$$

These were later found to be convertible into molecular complexes [45], such as seven coordinate $NdI_2(THF)_5$; eight coordinate $DyI_2(DME)_3$ and seven coordinate $TmI_2(DME)_3$ (note the lanthanide contraction at work).

Over the past half-century, these developments have been followed by a developing chemistry of the +2 state in lanthanide organometallic chemistry, most notably research carried out by Evans on Sm(II) compounds like $[Sm(C_5Me_5)_2]$ [46]. This has paled by comparison with Evans' most recent work, showing that the +2 state is accessible for all lanthanides, provided that the right ligand set is used, in the right geometry [47].

'Flash' reduction of $[Ln(C_5H_4SiMe_3)_3]$ using KC_8 on a column at -35-C, with all isolation steps carried out at that temperature, leads to $[K(18\text{-crown-6})][Cp'_3Ln]$ (Ln = Y, La-Nd, Sm-Lu; Figure 6) and also $[K(2.2.2\text{-cryptand})][Cp'_3Ln]$ ($Cp' = C_5H_4SiMe_3$). Study of the magnetic and spectroscopic properties of these compounds indicates that the Sm, Eu, Tm and Yb compounds have f^n electron configurations, whilst the compounds of La-Nd, Gd-Er and Lu are have $f^{n-1}d^1$ electron configurations. So the electronic ground state of the Dy(II) and Nd(II) compounds depend on the ligand environment, something unprecedented in lanthanide chemistry, as the $[Cp'_3Ln]^-$ ions

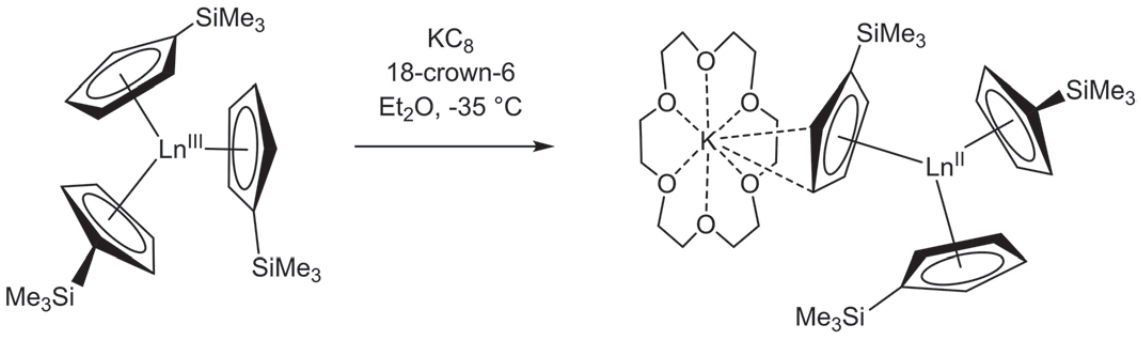

Figure 6. Synthesis of the Ln(II) compounds $[K(18\text{-crown-6})][Cp'_3Ln]$

of Dy^{2+} and Nd^{2+} are $4f^9\ 5d^1$ and $4f^3\ 5d^1$, respectively, whereas in earlier compounds like $[NdI_2(THF)_5]$ and $[DyI_2(DME)_3]$ they are $4f^{10}$ and $4f^4$ respectively. The $C_5H_4SiMe_3$ ligand has created an environment such that – for the first time ever – the electronic ground state of a particular lanthanide ion can be changed by changing its environment. The choice of the cyclopentadienyl ligand is important, as the corresponding $[Cp'''_3Ln]^-$ ion ($[C_5H_3(SiMe_3)_2]$ = (Cp″)) has only been obtained for Ln = La, Ce, Pr, Nd [48]; likewise, the $[Cp^{tet}_3Ln]^-$ ion has been isolated for Ln = La, Ce, Pr, Nd, Sm, Gd, Tb, and Dy ($Cp^{tet} = C_5Me_4H$) [49].

Magnetism

The past half century has seen lanthanide-based magnets replace traditional iron-containing magnets in many applications. They produce stronger magnetic fields, owing to the higher magnetic moments of the lanthanides. The two main materials concerned are $SmCo_5$ and $Nd_2Fe_{14}B$. The former is more expensive but can operate at higher temperatures than the cheaper $Nd_2Fe_{14}B$. Both are more brittle than the robust iron magnets. Their higher strength means that they are more compact. Modern motor cars use them in many devices, notably traction motors in electric cars, as do computer hard drives, headphones and wind turbines [50].

Lanthanide containing single molecule magnets (SMMs) are an active area of research. They exhibit supermagnetic behaviour below a certain temperature (the 'blocking temperature') and are potentially magnetic memory units, capable of making up a quantum computer [51]. Materials like $[Dy(Cp^{ttt})_2][B(C_6F_5)_4]$ (Cp^{ttt}=1,2,4-tri(*tert*-butyl)cyclopentadienide) show promise [52], with blocking temperatures above 50K, though materials operating at liquid nitrogen temperatures and above are actively being sought.

All the Ln^{3+} except for La^{3+} and Lu^{3+} ions are paramagnetic, in some cases very strongly so. The most important application of this in recent years has been the use of gadolinium complexes in magnetic resonance imaging (MRI) agents used

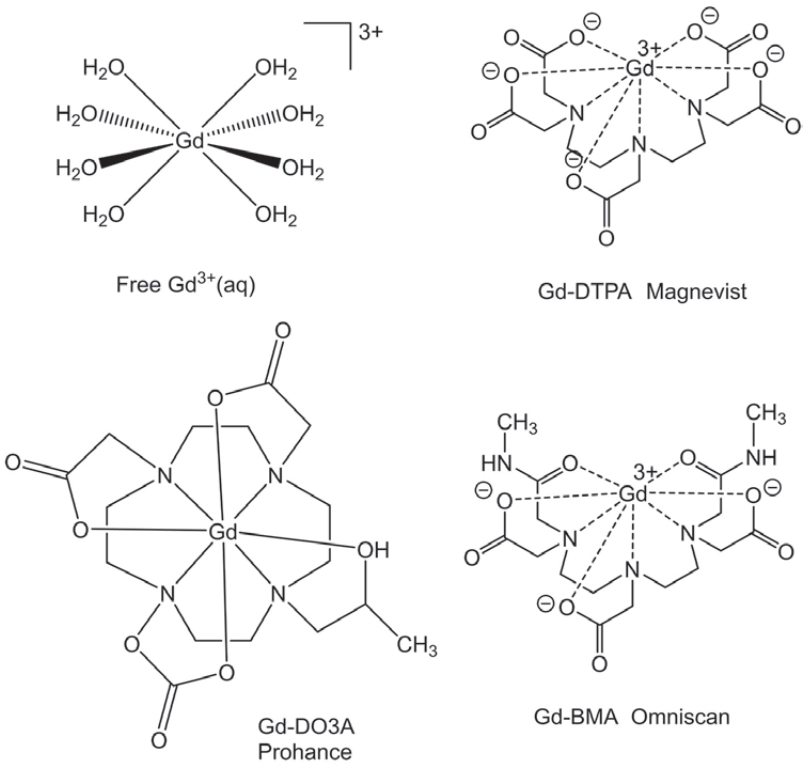

Figure 7. The structures of the gadolinium aqua ion, too toxic to be used in MRI, and three commercial MRI agents.

in medical diagnosis [53, 54]. MRI scanners are essentially pulsed NMR spectrometers, detecting signals from ^{1}H nuclei in water molecules; the contrast agents improve the images of bodily organs and structures, like tumours and blood supply. They work by shortening the relaxation times of ^{1}H nuclei inside tissues, and differentiate between healthy and diseased tissue. Free $Gd^{3+}(aq)$ is too toxic for use, so gadolinium complexes are required. Structures of some of these are shown in Figure 7.

For their first twenty years of use, MRI agents were regarded as totally safe. Recently, complications have emerged with patients with renal failure, so that with these patients MRI scans have been restricted. There has also been concern about Gd^{3+} deposition in neural tissues, including the brain (even in people with intact blood-brain barriers and normal renal functions) and the use of the more stable macrocyclic contrast agents promoted [55].
The latest development in magnetic materials lies in certain layered ceramic compounds, called MAX phases, incorporating certain rare earth elements [56]; this family of compounds has the general formula $[(Mo_{2/3}Ln_{1/3})_2AlC]$ (Ln = Ce, Pr, Nd, Sm, Gd, Tb, Dy, Ho, Er, Tm, and Lu) and exhibits "a plethora of ground states, resulting from an interplay of competing magnetic interactions in the presence of magnetocrystalline anisotropy". They have the potential of being used in future spintronics applications.

Catalysts

Lanthanides have a number of important applications, several on a large scale. Lanthanum and cerium are added to zeolite cracking catalysts in the petrochemical industry [57]. Because of its ability to switch oxidation states between +3 and +4, cerium is widely used in oxidation catalysts, often as CeO_2. Thus in self-cleaning ovens the CeO_2 catalyst oxidises molecules like fatty acids [58]. Cerium oxide is used in automobile three-way catalysts (TWC), not least as an oxygen store to smooth out the oxidising performance of the system. Its role includes improving low-temperature performance. Cerium oxide nanoparticles have been widely employed as a diesel fuel additive in vehicles, with a view to catalysing the regeneration of particulate filters through oxidising soot particles. Diesel particulate emissions are reduced, but there is concern over metallic nanoparticle emissions [59].

Lanthanides in Biology

Until recently, it was a given that the rare earth elements had no function in any living system. Yet had been known for years that some properties of the lanthanides resembled other metal ions, and it was commonplace to use them as spectroscopic probes for 'silent' ions (e.g. Ca^{2+}) - Eu^{3+} for its luminescence for example. In 2011, however, it was reported that XoxF, a methanol dehydrogenase (MDH) protein that converts methanol into methanal as an energy source, was lanthanide-dependent (and indeed was expressed when lanthanides were added to a culture medium) [60]. Shortly afterwards it was found that the thermoacidophilic bacterium *Methylacidiphilum fumariolicum SolV*, isolated from a volcanic mudpot in Italy, needed lanthanides to exist, and in 2014 the crystal structure [61] of XoxF isolated from *Methylacidiphilum fumariolicum SolV* showed cerium ions at the active site (structures of lanthanum and europium analogues have also been reported). In many ways, such as the aminoacid ligands utilised, it strongly resembles Ca^{2+}-dependent MDH enzymes, but with one extra carboxylate ligand, resulting in an increase in coordination number to 9, from 7 in Ca-MDH. It is believed to be widespread in marine environments.

The coordination sphere of the lanthanides (Figure 8) includes four amino acids, as well as the redox cofactor pyrroloquinoline quinone (PQQ), and an active site that binds the methanol. The lanthanides appear to act as Lewis acids; despite the fact that the later, smaller, lanthanides are stronger Lewis acids, early lanthanides are preferred by these organisms. This may mean that the organisms came to acquire and use the more abundant early lanthanides like La and Ce.
Lanmodulin, a protein more recently identified in the lanthanide-dependent *Methylobacterium extorquens,* binds lanthanides at picomolar levels,

with 10^8 fold selectivity for La^{3+} over Ca^{2+}. It has been suggested that there exists a Ln^{3+} uptake system that uses a chelator analogous to the use of sideropheres by bacteria wanting to acquire Fe^{3+}. When lanmodulin binds lanthanides, it undergoes a considerable conformational change from a substantially disordered state to a very compact one [62]. There is a growing interest in this scientific area which continues to develop [63].

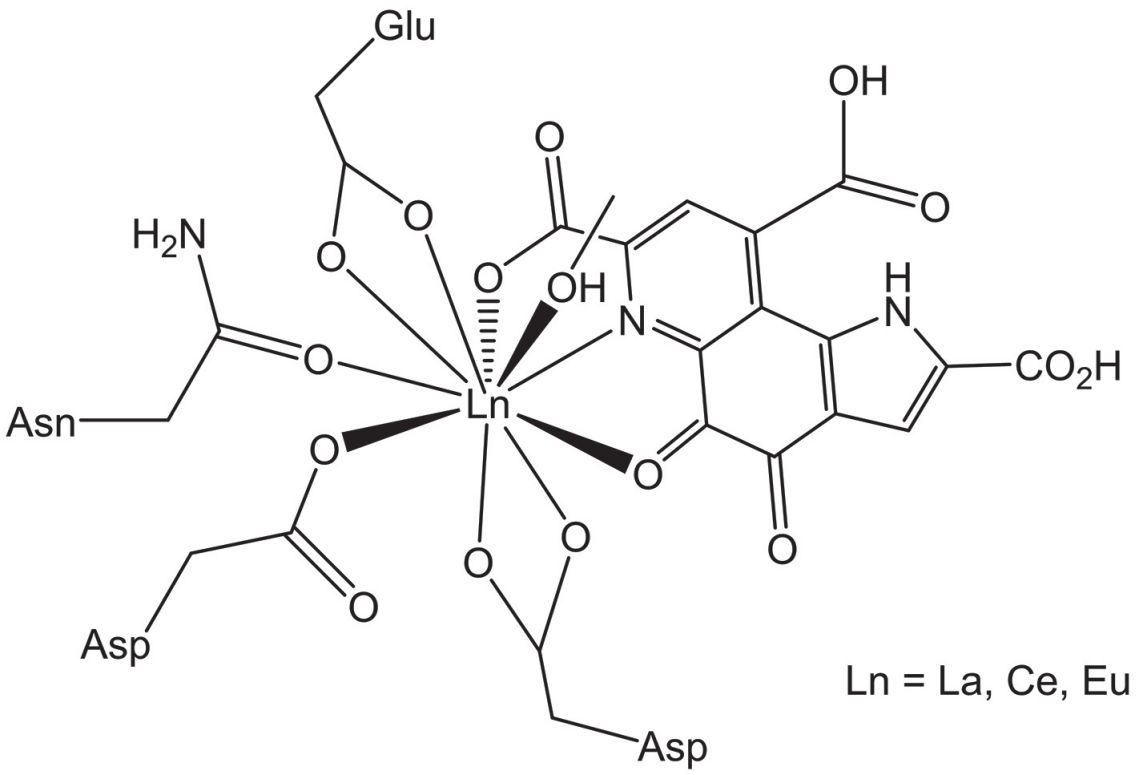

Fig. 8. The coordination sphere in the lanthanide-dependent MDH enzymes, with methanol substrate bound to the lanthanide (MDH = methanol dehydrogenase).

References

[1] Z. Chen, *J. Rare Earths*, **2011**, *29*, 1-6.

[2] B. S. Van Gosen, P. L. Verplanck, R. R. Seal, K. R, Long and J. Gambogi, **2017**, Rare-earth elements, chap. O *of* K. J. Schulz, J. H. DeYoung, R. R. Seal and D.C. Bradley, eds., Critical mineral resources of the United States—Economic and environmental geology and prospects for future supply: U.S. Geological Survey Professional Paper 1802, p. O1–O31, https://doi.org/10.3133/pp1802-O.

[3] D. Mendeleev, *Zeitschrift für Chemie*, **1869**, *12*, 405-406.

[4] D. Mendeleev, *Ann. Chem. Pharm*., **1872**, *Suppl. 8*, 133-229.

[5] H. G. J. Moseley, *Phil. Mag*., **1913**, *26*, 1024-1034; **1914**, *27*, 703-713.

[6] J. A. Harris and B. S. Hopkins, *J. Am. Chem. Soc*., **1926**, *48*, 1585-1594; L. Rolla and L. Fernandes, *Z. Anorg. Allg. Chem*., **1926**, *157*, 371-381; I. Noddack, *Angew. Chem*., **1934**, *47*, 301-305.

[7] (a) J. A. Marinsky, L. E. Glendenin and C. D. Coryell, *J. Am. Chem. Soc*. **1947**, *69*, 2781–2785; (b) M. V. Orna, *The Lost Elements*, Oxford, Oxford University Press, **2014**, pp 294-310.

[8] C. James, *J. Am. Chem. Soc.*, **1911**, *33*, 1332-1344.

[9] T. Cheisson and E. J. Schelter, *Science*, **2019**, *363*, 489–493.

[10] F. Xie, T. A. Zhang, D. Dreisinger and F. Doyle, *Minerals Engineering*, **2015**, 56, 10-28.

[11] V. M. Goldschmidt, T. Barth and G. Lunde, "Geochemische Verteilungsgesetze der Elemente", Part V "Isomorphie und Polymorphie der Sesquioxyde. Die Lanthaniden-Kontraktion und ihre Konsequenzen", Skrifter Norske Videnskaps-Akademi i, Oslo, **1925**.

[12] S. A. Cotton and P. R. Raithby, *Co-ordination Chem. Revs*., **2017**, *340*, 220-231.

[13] E. Constable and C. E. Housecroft, *Chem. Soc. Rev*., **2013**, *42*, 1429-1439.

[14] (a) J. A. A. Ketelaar, *Physica*, **1937**, *4*, 619 – 630; (b) L. Helmholz, *J. Am. Chem. Soc*., **1939**, *61*, 1544-1550.

[15] A. Zalkin, J. D. Forrester and D. H. Templeton, *J. Chem. Phys*., **1963**, *39*, 2881-2891.

[16] J. L. Hoard, B. Lee and M. D. Lind, *J. Am. Chem. Soc*., **1965**, *87*, 1612–1613.

[17] R. Janicki and A. Mondry, *Phys. Chem. Chem. Phys*., **2014**, *16*, 26823-26831.

[18] A. Chatterjee, E. N. Maslen and K. J. Watson, *Acta Cryst.* **1988**, *B44*, 381-386.

[19] J. Glaser and G. Johansson, *Acta Chem. Scand*., **1981**, *A35*, 639-644.

[20] Chunhui Huang (ed.), *Rare Earth Coordination Chemistry: Fundamentals and Applications*, Singapore, John Wiley, **2010**, p. 18.

[21] E. C. Alyea, D. C. Bradley and R. G. Copperthwaite, *J. Chem. Soc., Dalton Trans*.**,** 1972, 1580-1584.

[22] (a) J. S. *Ghotra*, M. B. *Hursthouse* and A. J. *Welch*. J. Chem. Soc., Chem. Commun., **1973**, 669-670; (b) D. C. Bradley, J. S. Ghotra and F. A. Hart, *J. Chem. Soc., Dalton Trans*., **1973**, 1021-1023.

[23] E. D. Brady, D. L. Clark, J. C. Gordon, P. J. Hay, D. W. Keogh, R. Poli, B. L. Scott, and J. G. Watkin, *Inorg. Chem*., **2003**, *42*, 6682-6690.

[24] S. A. Cotton, F. A. Hart, M. B. Hursthouse and A. J. Welch, *J. Chem. Soc. Chem. Comm*., **1972**, 1225-1226.

[25] C. Eaborn, P. B. Hitchcock, K. Izod and J. D. Smith, *J. Am. Chem. Soc*., **1994**, *116*, 12071-12072.

[26] G. Urbain and E. Budischovsky, *Compt. Rend*., **1897**, *124*, 618-621.

[27] K. Binnemans, *Handbook on the Physics and Chemistry of Rare Earths*, **2005**, *35*, 107-272.

[28] H. Shen, A. S. Berezin , O. V. Antonova , V. V. Zvereva , I. V. Korolkov, N. V. Pervukhina, S. A. Prokhorova , and P. A. Stabnikov, *J. Struct. Chem*., **2018**, *59*, 676-683.

[29] (a) A. L. Johnson and J. D. Parish, *Organomet. Chem*., **2019**, *42*, 1–53; (b) H.-L. Hsu, K. R. Leong, I.-J. Teng, M. Halamicek, J.-Y. Juang, S.-R. Jian, L. Qian and N. P. Kherani, *Materials,* **2014**, *7*, 1539–1554.

[30] C. C. Hinckley, *J. Am. Chem. Soc.*, **1969**, *91*, 5160-5162.

[31] T. J. Wenzel, *NMR Shift Reagents*, Boca Raton, Florida, CRC Press, **1987**.

[32] G. H. Dieke, *Spectra and Energy Levels of Rare Earth Ions in Crystals*, edited by H. M. Crosswhite and H. Crosswhite, New York, Interscience, **1968**, pp.249–253.

[33] J.-C. G. Bünzli, *Trends in Chemistry*, **2019**, *1*, 751-762.

[34] D. G. Karraker, *Inorg. Chem.,* **1968**, *7*, 473-479.

[35] J. Lucas, P. Lucas, T. Le Mercier, A. Rollat and W. G. I. Davenport, *Rare Earths: Science,*

Technology, Production and Use, Amsterdam, Elsevier, **2015**, pp. 319-332.

[36] G. Urbain, C. *R. Acad. Sci. Paris,* **1906***, 142*, 205–207.

[37] S. I. Weissman, *J. Chem. Phys*., **1942**, *10*, 214–217.

[38] T. Sano, M. Fujita, T. Fujii, Y. Hamada, K. Shibata and K. Kuroki, *Jpn. J. Appl. Phys*. **1995**, *34*, 1883-1887.

[39] M. L. Cable, J. P. Kirby, D. J. Levine, M. J. Manary, H. B. Gray and A. Ponce, *J. Am. Chem. Soc.,* **2009**, *131*, 9562–9570.

[40] (a) S. V. Eliseeva and J.-C. G. Bünzli, *Chem. Soc. Rev*., **2010**, *39*, 189–227; (b) J.-C. G. Bünzli, *Eur. J. Inorg. Chem.,* **2017**, 5058–5063.

[41] (a) A. Werner, *Ber. Dtsch. Chem. Ges.,* **1905**, *38*, 914-921; (b) P. J. Stewart, *Found. Chem*., **2019**, *21*, 3–9.

[42] D. A. Johnson and P. G. Nelson, *Found Chem*., **2018**, *20*, 15–27.

[43] C. Matignon and E. C. Cazes, *Ann. Chim. Phys*., **1906**, *8*, 417-426; F. Bourion and G. Urbain, *Compt. Rend*, **1911**, *153*, 1155- 1158; W. Klemm and G. Schüth, *Z. Anorg. Allg. Chem*., **1929**, *184*, 352-358.

[44] L. F. Druding and J. D. Corbett, *J. Am. Chem. Soc*., **1959**, *81*, 5512; L. B. Asprey and F. H. Kruse, *J. Inorg. Nucl. Chem*., **1960**, *13*, 32 – 35.

[45] (a) W. J. Evans, N. T. Allen and J. W. Ziller, *J. Am. Chem. Soc*., **2000**, *122*, 11749−11750; (b) M. N. Bochkarev, *Coord. Chem. Rev*., **2004**, *248*, 835−851 and references therein.

[46] (a) W. J. Evans, L. A. Hughes and T. P. Hanusa, *Organometallics*, **1986**, *5*, 1286-1291; (b) https://www.chem.uci.edu/~wevans/Evans_Lab/decamethylsamarocene.html

[47] W. J. Evans, *Organometallics*, **2016**, *35*, 3088−3100.

[48] C. T. Palumbo, L. E. Darago, C. J. Windorff, J. W. Ziller and W. J. Evans, *Organometallics*, **2018**, *37*, 900-905.

[49] T. F. Jenkins, D. H. Woen, L. N. Mohanam, J. W. Ziller, F. Furche and W. J. Evans, *Organometallics,* **2018**, *37*, 3863-3873.

[50] J. D. Widmer, R. Martin and M. Kimiabeigi, *Sustainable Materials and Technologies*, **2015**, *3, 7-13.*

[51] J. Luzon and R. Sessoli, *Dalton Trans*., **2012**, *41*, 13556-13567; D. N. Woodruff, R. E. P. Winpenny and R. A. Layfield, *Chem. Rev.*, **2013**, *113*, 5110–5148.

[52] C. A. P. Goodwin, F. Ortu, D. Reta, N. F. Chilton and D. P. Mills, *Nature*, **2017**, *548*, 439-442; F.-S. Guo, B. M. Day, Y.-C. Chen, M.-L. Tong, A. Mansikkamäki and R. A. Layfield, *Angew. Chem. International Ed.,* **2017**, *56*, 11445–11449.

[53] P. Caravan, J. J. Ellison, T. J. McMurry and R. B. Lauffer, *Chem Rev*., **1999**, *99*, 2293–2352.

[54] *The Chemistry of Contrast Agents in Medical Magnetic Resonance Imaging*, A. Merbach, L. Helm and E. Tóth, eds., 2nd edition, Chichester, John Wiley, **2013**.

[55] D. V. Bower, J. K. Richter, H. von Tengg-Kobligk, J. T. Heverhagen and V. M. Runge, *Invest. Radiol*., **2019**, *54*, 453–463.

[56] Q. Tao, *et al. Chem. Mater*., **2019**, *31*, 2476-2485.

[57] M. Dejhosseini *et al*., *Energy Fuels*, **2013**, *27*, 4624−4631.

[58] P. Palmisaro *et al*., *Chem. Eng. J*., **2009**, *154*, 251-257.

[59] Z.-H. Zhang and R. Balasubramanian, *Environ. Sci. Technol*., **2017,** *51*, 4248-4258 and references therein.

[60] Y. Hibi, K. Asai, H. Arafuka, M. Hamajima, T. Iwama, K. Kawai, *J. Biosci. Bioeng*., **2011**, *111*, 547 – 549.

[61] A. Pol, T. R. M. Barends, A. Dietl, A. F. Khadem, J. Eygensteyn, M. S. M. Jetten, H. J. M. Op den Camp, *Environ. Microbiol*., **2014**, *16*, 255 – 264.

[62] J. A. Cotruvo, E. R. Featherston, J. A. Mattocks, J. V. Ho and T.N. Larmore, *J. Am. Chem. Soc*. **2018**, *140*, 15056−15061.

[63] (a) L. J. Daumann, *Angew. Chem. Int. Ed*., **2019**, *58,* 12795-12802; (b) J. A. Cotruvo, *ACS Cent. Sci.,* **2019**, *5*, 1496-1506.

Jean Claude JODOGNE
Ir. Dr., Chef de département honoraire
consultant libre IRM, 3 Av.Circulaire - 1180 Bruxelles
jodjc63cm@gmail.com

Un nouveau tableau périodique conforme à la chimie quantique relativiste

À mon père, Joseph Jodogne, initiateur en 1962 de la première réforme fondamentale pour une Chimie déductive et non plus quelque peu apparentée à des recettes de cuisine, dans l'enseignement secondaire en Belgique francophone.

Résumé
Mettant à profit les progrès de la chimie quantique relativiste, une voie est proposée pour une représentation nouvelle basée sur les niveaux d'énergie des électrons dans l'état fondamental des atomes. Avec un nouveau paramètre de famille, on met alors en évidence de très nombreuses corrélations (similitudes ou périodes). Ce nouveau tableau permet d'avoir une disposition très voisine de celle, historique du tableau usuel mais bénéficie de plus d'avantages pour son usage en chimie.

A new periodic table according to relativistic quantum Chemistry

Abstract
Relativistic quantum Chemistry progresses permit a new way to the periodic table's representation taking into account energy levels of electrons in atom's ground state. Use of a new family parameter shows then a lot of correlations (similarities thus periods). This new table allows to have a display similar to the historical one of the usual periodic table but has more advantages when using it in Chemistry.

Keywords
Periodic Table, Family, Quantum Chemistry

1. Introduction

À la lumière des idées de ses précurseurs, Dmitri Mendeleïev, tenant compte de la parenté de comportement de certains composés chimiques, a pu classer les atomes connus à son époque, par rapport à leur masse atomique (Figure 1). Avec 63 éléments, il a remarquablement prévu l'existence de quelques atomes manquants dans ses suites d'atomes, atomes qu'il appelait éléments « réels » pour les distinguer de la substance.

Pour arriver à un classement suivant la charge du noyau au lieu de la masse atomique, il a fallu attendre les recherches et la proposition de l'anglais Henri Moseley (1913). Celui-ci prédit l'existence de quatre atomes alors inconnus (de Z = 43, 61, 72 et 75). Suite au bombardement de l'azote par des particules alpha, la découverte des protons émis initia l'idée de l'existence de ceux-ci dans le noyau de l'atome.

En avril 1928, un chimiste français, Charles Janet présenta le premier Tableau Périodique (TP) en blocs dans l'ordre spdf (de dr. à g.). Il était ordonné suivant Z mais très étendu en largeur. La troisième version publiée en novembre (Figure 2) [1] corrige la première où la ligne 1 était composée des quatre premiers atomes et où tous les atomes ayant un nombre quantique $\ell = 0$ étaient décalés d'une ligne vers le haut par rapport au TP usuel.

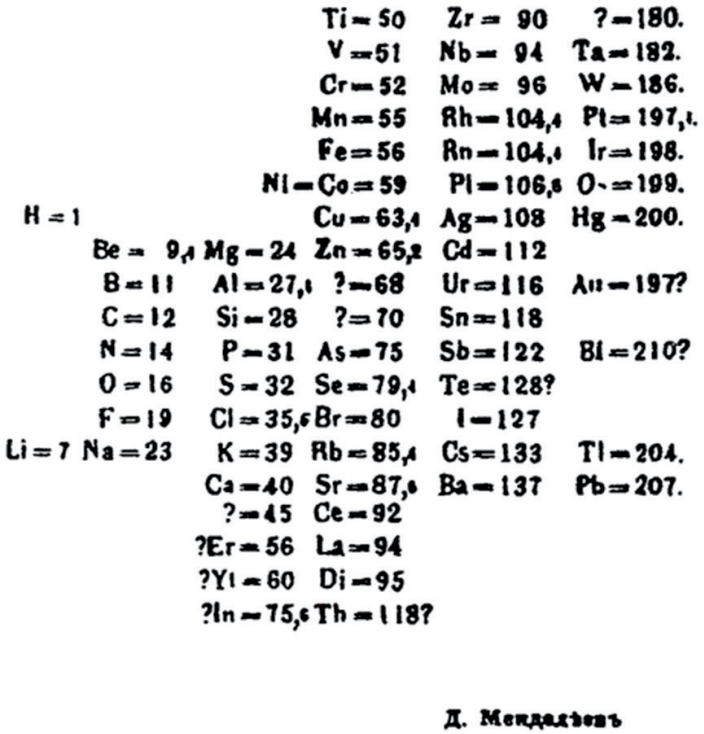

			Ti = 50	Zr = 90	? = 180.	
			V = 51	Nb = 94	Ta = 182.	
			Cr = 52	Mo = 96	W = 186.	
			Mn = 55	Rh = 104,4	Pt = 197,1.	
			Fe = 56	Ru = 104,4	Ir = 198.	
			Ni = Co = 59	Pl = 106,6	Os = 199.	
H = 1			Cu = 63,4	Ag = 108	Hg = 200.	
	Be = 9,4	Mg = 24	Zn = 65,2	Cd = 112		
	B = 11	Al = 27,4	? = 68	Ur = 116	Au = 197?	
	C = 12	Si = 28	? = 70	Sn = 118		
	N = 14	P = 31	As = 75	Sb = 122	Bi = 210?	
	O = 16	S = 32	Se = 79,4	Te = 128?		
	F = 19	Cl = 35,6	Br = 80	I = 127		
Li = 7	Na = 23	K = 39	Rb = 85,4	Cs = 133	Tl = 204.	
		Ca = 40	Sr = 87,6	Ba = 137	Pb = 207.	
		? = 45	Ce = 92			
		?Er = 56	La = 94			
		?Yt = 60	Di = 95			
		?In = 75,6	Th = 118?			

Д. Менделѣевъ

Figure 1. Un des tableaux de Mendeleïev (extrait de Wikipedia)

Après la découverte par réactions nucléaires de nombreux nouveaux atomes radioactifs, Glenn Seaborg en 1944, donna sa forme actuelle au TP et y ajouta la série des atomes révélés (les actinides). Les propriétés de ces derniers en rapport avec la périodicité chimique étant peu ou pas connues, il est sans doute prématuré d'établir leurs contributions à cette dernière.

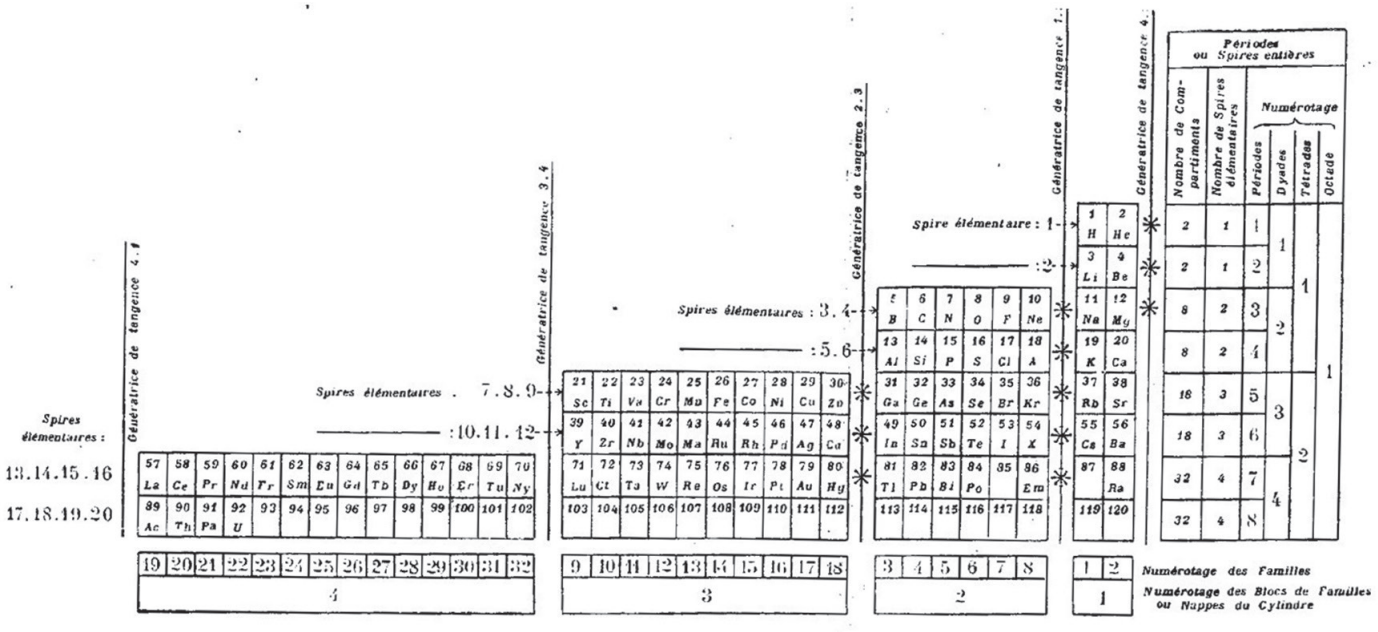

Figure 2. Troisième version publiée en novembre 1928 avec des renvois vers la représentation en spirale

Plus d'un millier de représentations du TP existent mais aucune de celles-ci ne tient compte des progrès récents de la Chimie Quantique (CQ). Déjà en 1975, E.G. Mazurs, auteur d'un livre remarquable sur les représentations du tableau, écrivait [2] : « The time has come to accept the electronic structure tables ». Au XXI^{e} siècle, le tableau de l'IUPAC ne tient pas compte des progrès des connaissances récentes. Pour aborder la configuration électronique de chaque atome, il est tellement difficile de s'y retrouver que la solution généralement adoptée est de l'inscrire dans chaque case du tableau, de renvoyer vers un autre tableau ou encore d'utiliser les « couches » K, L, M… qui n'existent pas. La question posée est dès lors de trouver une représentation qui tienne compte des progrès considérables des connaissances atomiques et moléculaires. Et que cette nouvelle représentation conserve l'idée capitale de Mendeleïev, celle qui a présidé à l'ordonnancement historique du tableau : la périodicité chimique.

2. Construire un tableau des éléments tenant compte des idées actuelles

Ces dernières années, la chimie théorique et en particulier, la chimie computationnelle a accompli des progrès remarquables en démontrant l'impact de la Mécanique Quantique (MQ) mais aussi de la MQ relativiste, sur la compréhension des éléments chimiques. Ces développements tendent à montrer que la MQ est, jusqu'à présent, le meilleur modèle.

*La configuration électronique de l'atome comme base de départ **a priori***

La MQ décrit les électrons dans l'atome par des fonctions d'onde. Mais dès qu'il y a plus d'un électron, cela devient un problème à plusieurs corps. Pour contrer cette difficulté, l'approche est alors d'utiliser une combinaison linéaire (orbitale) des solutions relatives aux ions qui ne possèdent plus qu'un seul électron (atomes hydrogénoïdes). À ces fonctions d'onde correspondent des **niveaux d'énergie** de l'électron dans l'atome, chaque électron ayant un seul jeu distinct de quatre nombres quantiques n, ℓ, m et s. Ces nombres quantiques satisfont à des règles très simples ; celles des deux premiers sont essentielles pour le TP :

n, ℓ = premiers entiers positifs et $\ell < n$.

Les nouveaux développements en CQ sont décrits par exemple à la Ref. [3]. Dans l'article de Hiroshi Nakatsuji [4] une méthode générale pour résoudre les équations quantiques atomiques et moléculaires est proposée. Mais il faut aussi tenir compte des progrès récents de la CQ relativiste. En effet, les travaux de Pekka Pyykkö [5] ont montré que quelques niveaux d'énergie calculés par le modèle hydrogénoïde doivent être ajustés quand on considère les atomes neutres (avec autant d'électrons que de protons). Sauf ceux des niveaux n = 1 et 2 qui ne changent pas, ces quelques premiers niveaux d'énergie sont représentés à la Figure 3 avec l'énergie croissante vers le haut et les nouvelles positions des niveaux (en rouge). Pour l'édification du TP, il en résulte que le principe H-like Aufbau doit être remplacé par le principe Real Aufbau (tableau 1 [5]).

Dans l'état fondamental des différents atomes, les électrons vont occuper les niveaux d'énergie la plus basse. Lors de la progression en Z, la séquence de succession des électrons sur ces niveaux se réalise vers ceux d'énergie de plus en plus élevée puisque les niveaux d'énergie plus basse sont les premiers remplis. Ainsi, lors du passage d'un atome Z à l'atome Z+1, l'électron additionnel occupera soit le même sous-niveau (pour n et ℓ déterminés) que l'électron ajouté pour l'atome Z s'il y a encore de la place, soit la première place du sous-niveau d'énergie immédiatement supérieur (le nombre de places est équivalent à 2 fois 2 ℓ + 1). Dans la présentation des éléments, si nous adoptons l'idée de placer les cases des atomes sur des segments horizontaux dans l'ordre de la hiérarchie du Real Aufbau des niveaux d'énergie, la continuité de la succession selon Z devient possible sans exception. En conséquence, la séquence en nombre atomique Z croissant suit alors exactement l'ordre croissant des niveaux d'énergie de l'atome Z dans son état fondamental. La succession des places des différents atomes est alors expliquée par l'état d'énergie minimale correspondant à l'état fondamental

de chaque atome. Elle suit la progression horizontale **et verticale** en Z comme le recommande Eric Scerri [5]. Le nombre atomique Z est le facteur d'agencement **logique**. Mais si Z progresse de gauche à droite et de bas en haut, cela conduit à un tableau d'allure inversée par rapport au tableau usuel [1]. On perdrait ainsi les familiarités d'usage déjà bien établies. Pour cette raison, le choix de la croissance de l'énergie des niveaux de l'atome vers le bas (Figure 4) sera adopté. Le nouveau tableau se présentera alors comme dans la Figure 5.

Un avantage considérable apparaît : les blocs s, p, d et f sont dans l'ordre logique. Dans un atome à l'état le plus stable, les électrons vont remplir les sous-niveaux les plus bas en énergie jusqu'à épuisement du nombre d'électrons. Lorsqu'on ajoute une charge au noyau, l'électron supplémentaire ne peut occuper qu'un sous-niveau non rempli sur le même sous-niveau que celui de l'électron ajouté à l'élément précédent ou si ce dernier sous-niveau est complet, sur celui immédiatement supérieur en énergie c'est-à-dire plus bas (à cause du choix de la progression en énergie vers le bas).

Remarquons que l'électron additionnel lors du passage de Z à Z+1, étant sur le sous-niveau le plus élevé en énergie, est le plus facile à extraire de l'atome (ionisation). Pour des raisons pratiques, sur le nouveau tableau, les écarts séparant les différents niveaux ne sont pas à l'échelle (Figure 6). Grâce à l'usage des couleurs, on indique les périodes par une ligne jaune, parfois brisée, au contact des cases et on suggère d'autres comportements chimiques traditionnels (métaux, semi-métaux, halogènes, gaz nobles…). La représentation du tableau proposée à la Figure 6 permet également de faire apparaître les familles du tableau, ce qui est essentiel pour faire ressortir la périodicité des propriétés chimiques des composés.

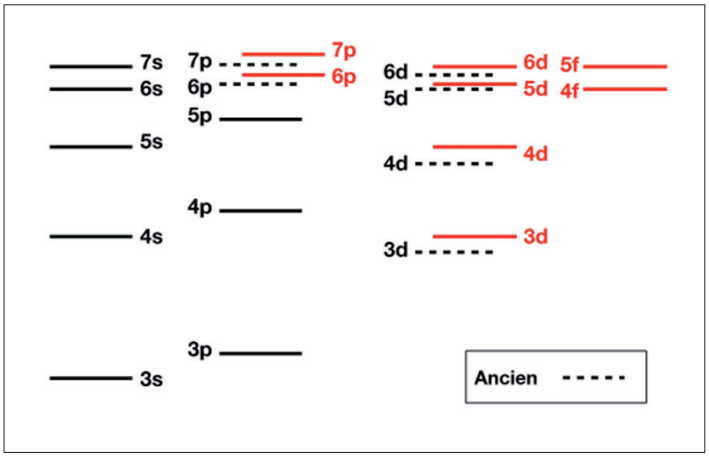

Figure 3. Niveaux d'énergie adaptés de la réf.5 (en rouge)

H-like Aufbau		Real Aufbau	
P Niveaux d'énergie	Nombre d'électrons	**P** Niveaux d'énergie	Nombre d'électrons
7 7s 7p 7d 7f 7g 7h 7i	98	**7** (7s 6d 5f) 7p	32
6 6s 6p 6d 6f 6g 6h	72	**6** (6s 5d 4f) 6p	32
5 5s 5p 5d 5f 5g	50	**5** (5s 4d) 5p	18
4 4s 4p 4d 4f	32	**4** (4s 3d) 4p	18
3 3s 3p 3d	18	**3** 3s 3p	8
2 2s 2p	8	**2** 2s 2p	8
1 1s	2	**1** 1s	2

Tableau 1. H-like Aufbau et Real Aufbau (entre parenthèses les niveaux égaux en énergie)

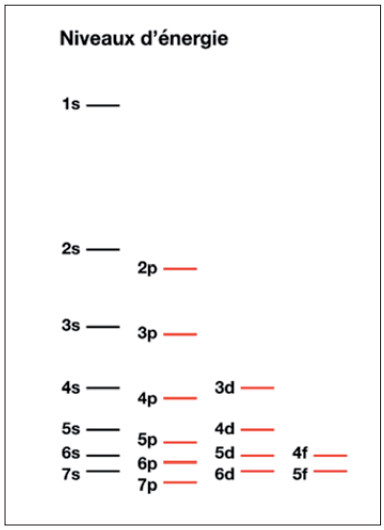

Figure 4. Niveaux avec l'énergie croissante vers le bas

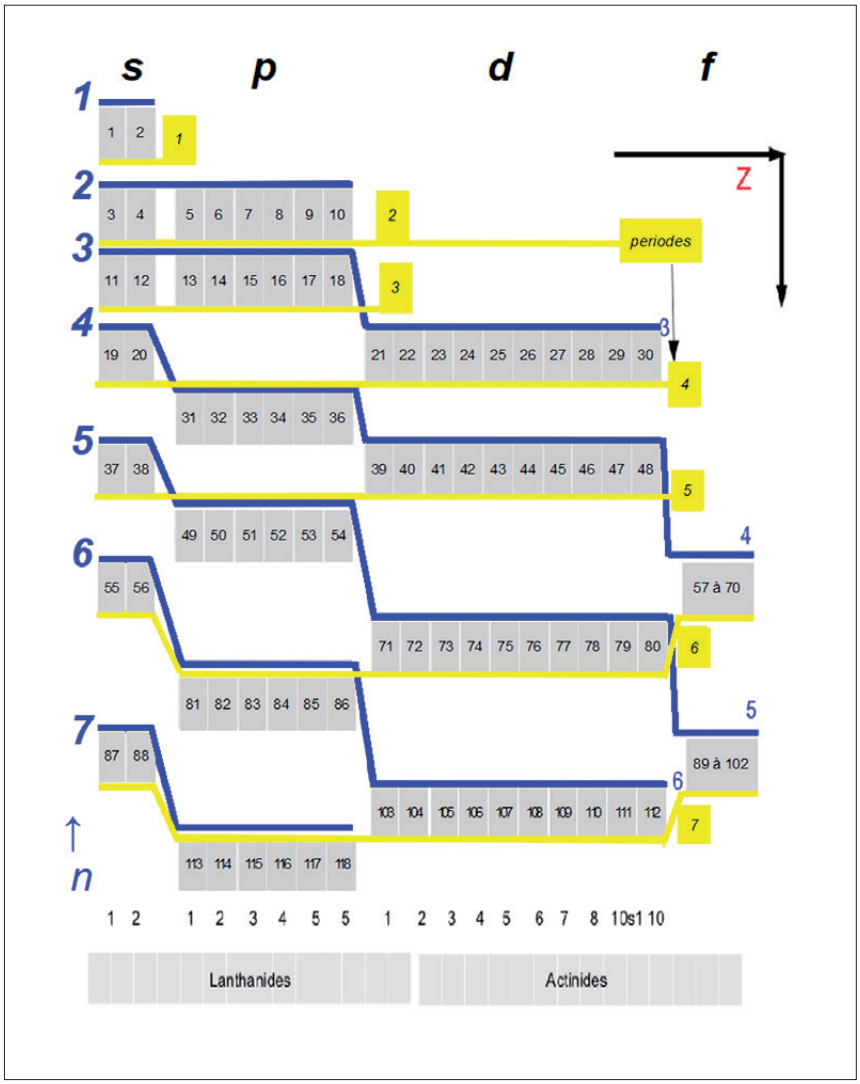

Figure 5. Disposition suivant les niveaux pour n>3

3. Inclure l'apport historique capital des périodes (similitudes)

Un grand bénéfice de cette nouvelle représentation est la mise en évidence facile de ces similitudes. Le nombre d'électrons présents au niveau principal d'énergie *n* qui se remplit suivant Z est un indicateur des corrélations (similitudes). Pour la facilité de l'exposé, appelons ce nombre : **paramètre de famille F**. On obtient facilement ce paramètre dans cette représentation. En effet, pour chaque nombre quantique principal *n* (ligne bleue), comme l'ordre des blocs est spdf, le nombre F est simplement le numéro d'ordre de la colonne de l'élément, numéro repris en haut du tableau. Ainsi, le paramètre de famille F du Ga est 3 = 2 + 1 (colonne 3), celui du W est 12 = 2 + 6 + 4.

Voyons maintenant comment ce paramètre est un révélateur pédagogique de la périodicité chimique, celle-ci étant une notion vague chez les apprentis chimistes. Mettant en graphique une série exemplaire de propriétés chimiques ou physico-chimiques en fonction de ce nouveau paramètre de famille, (la simple position de la colonne de l'atome) les figures suivantes de 7 à 15 sont éclairantes et nettement plus explicites des corrélations comparées aux graphiques en fonction de Z. Ces derniers ne permettent pas de voir l'existence de corrélation ou de famille. Au vu du seul tableau et sans formation en Chimie, le mot famille n'est qu'un mot.

La périodicité chimique mise en évidence par Mendeleïev est ainsi reliée à un paramètre simple relatif à la configuration électronique des atomes

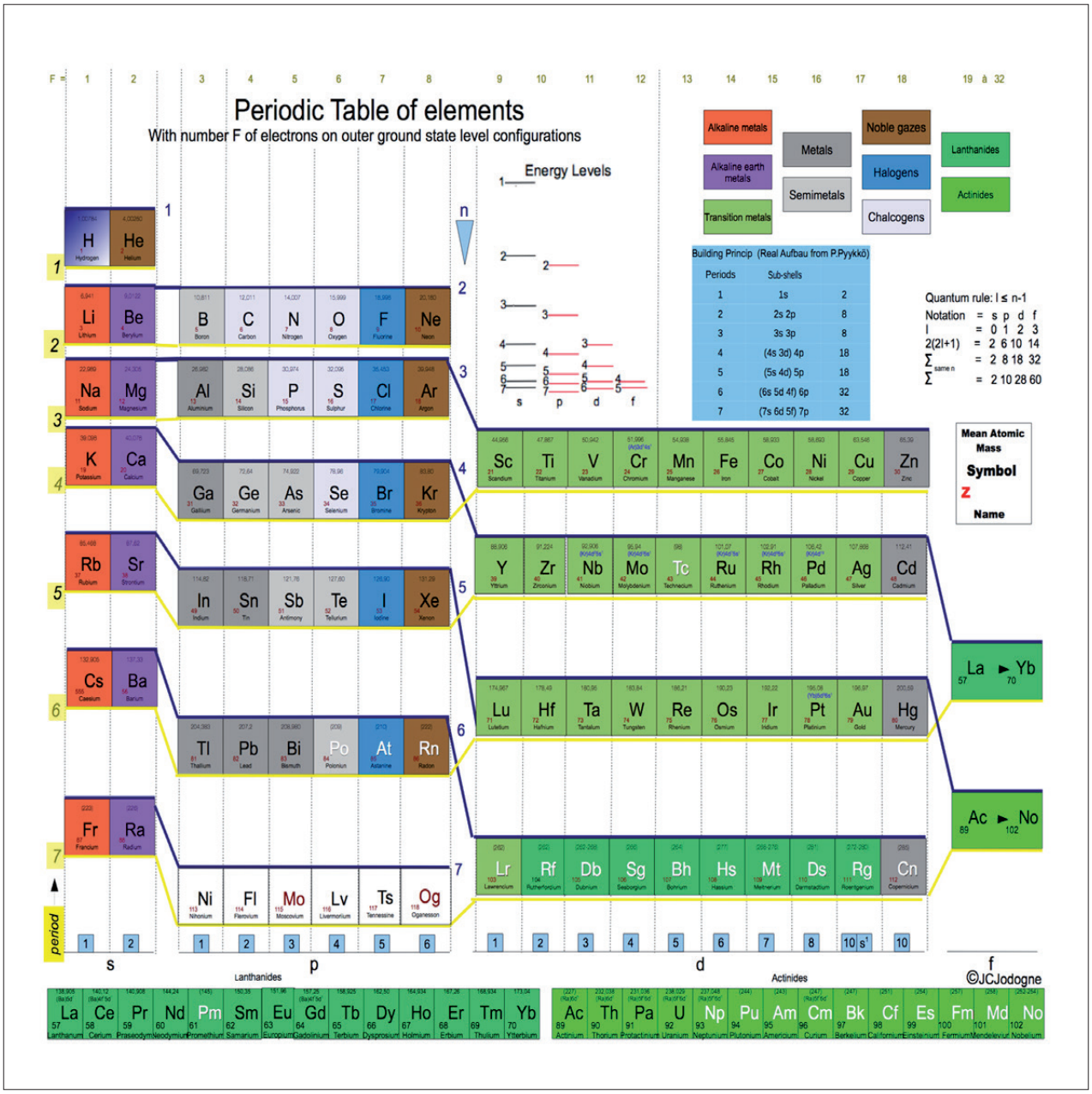

Figure 6. Le nouveau tableau avec l'apport essentiel des couleurs

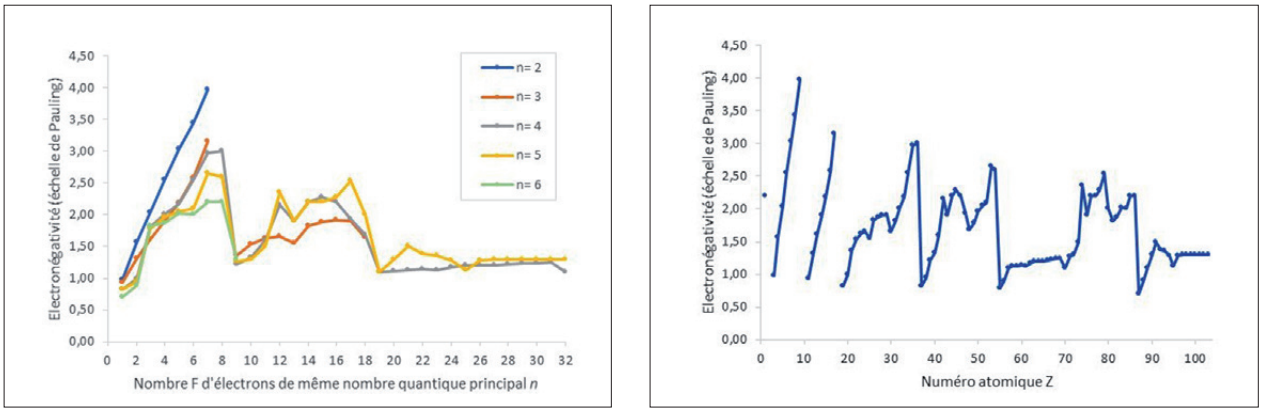

Figure 7. Electronégativités (échelle de Pauling) en fonction de F (gauche) et de Z (droite)

des éléments. Examinons la propriété d'électronégativité (Figure 7). Sur le graphique du haut, on perçoit clairement que, quel que soit le nombre quantique principal (> 1), cette propriété a sensiblement la même valeur pour la famille d'atomes de même valeur du paramètre F.

Essayons une autre propriété, l'énergie de première ionisation (Figure 8). Les valeurs sont presque les mêmes pour un même paramètre F alors que le graphique en Z est de nouveau moins démonstratif. Dans les figures suivantes, nous omettrons les graphiques en Z.

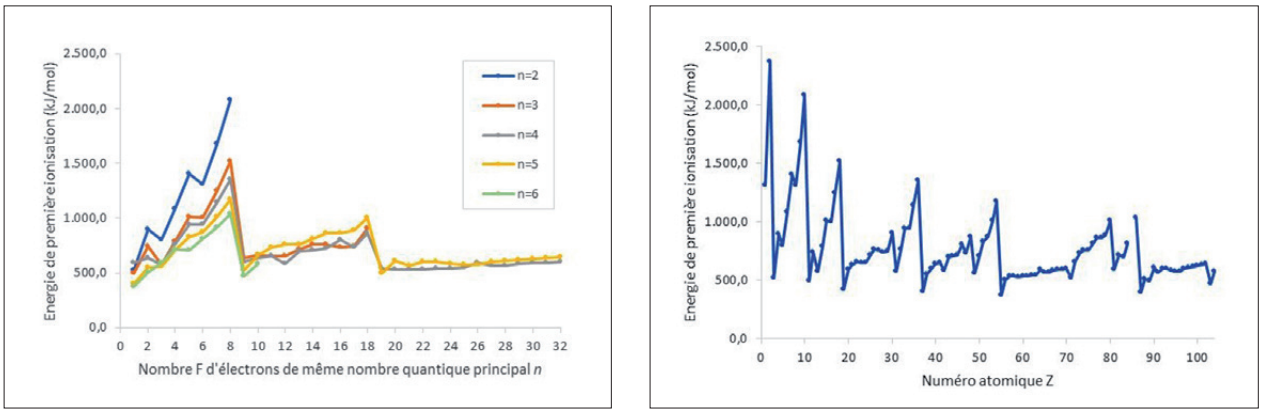

Figure 8. Energies de première ionisation en fonction de F (gauche) et de Z (droite)

Ces similitudes sont peut-être dues au hasard. Voyons des grandeurs liées à la température. Comment se placent les valeurs des températures de fusion (Figure 9) et d'ébullition (Figure 10) ainsi que les enthalpies respectives (Figures 11 et 12).

On retrouve la même allure générale alors que lors de la fusion ou de l'ébullition, il est clair que la configuration électronique n'est pas la seule cause de la valeur de ces propriétés. A l'état solide ou liquide, des liens particuliers existent. Lorsque le remplissage du sous-niveau est proche de la moitié (par ex. pour F = 11, …, 15), les valeurs des propriétés sont plus dispersées mais néanmoins, l'évolution pour les atomes avec même F est semblable pour chaque nombre quantique principal. Regardons encore comment se présente une propriété presque ignorée dans la recherche des similitudes, la tension superficielle à 25°C (Figure 13). Une nouvelle fois, il y a un air de famille sauf pour n = 2 et F = 2 ou 4 !

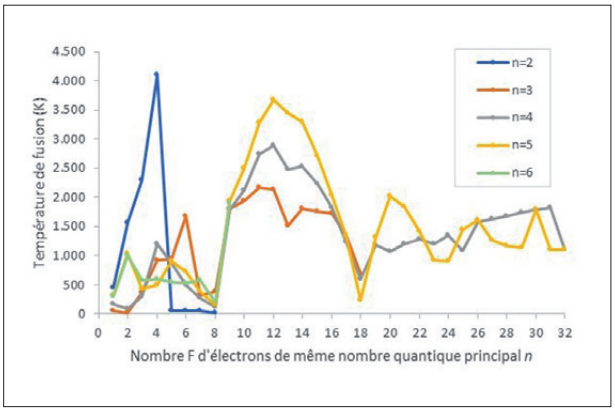

Figure 9. Températures de fusion en fonction de F

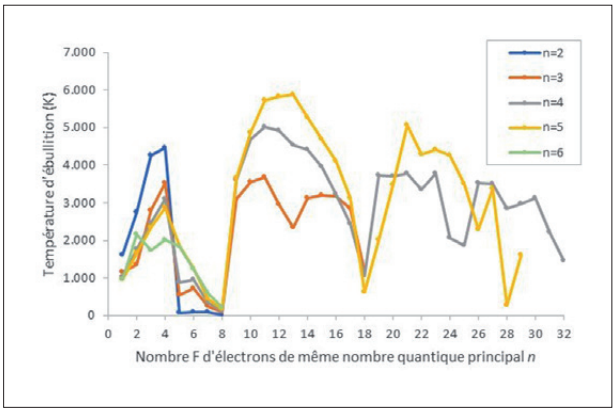

Figure 10. Températures d'ébullition en fonction de F

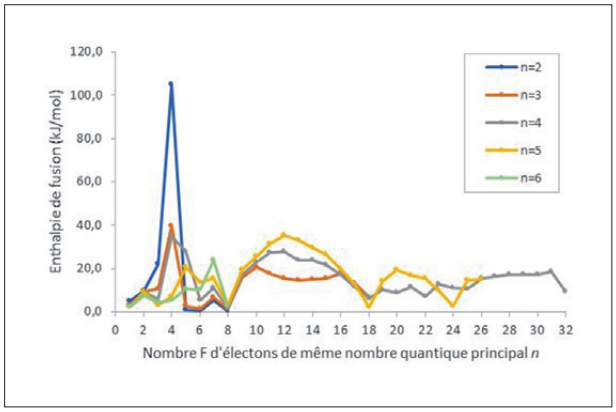

Figure 11. Enthalpies de fusion en fonction de F

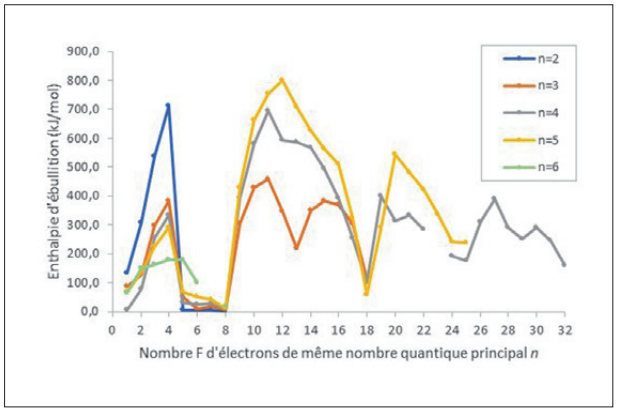

Figure 12. Enthalpies d'ébullition en fonction de F

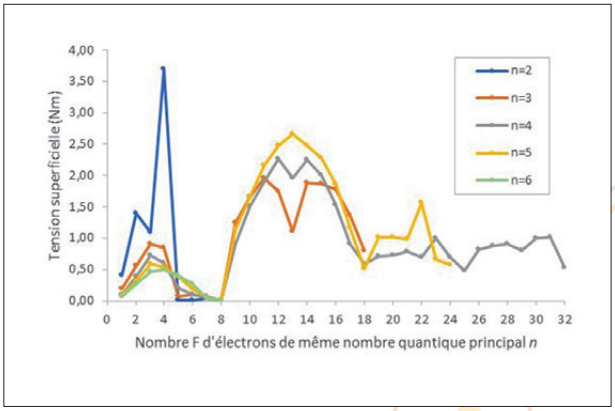

Figure 13. Tensions superficielles à 25°C en fonction de F

Ces similitudes seraient-elles valables pour des grandeurs liées à l'espace comme le volume molaire (Figure14) ou le rayon atomique mesuré (Figure 15) ?

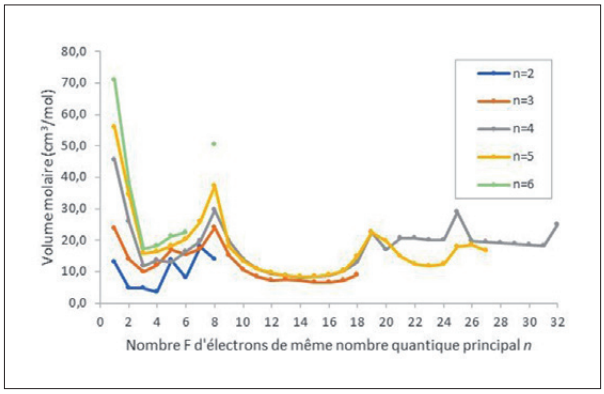

Figure 14. Volumes molaires en fonction de F

Pour les volumes molaires et les rayons atomiques mesurés, la régularité entre les éléments du bloc d est bien marquée. A nouveau, l'évolution de la grandeur examinée, ici le volume molaire (Figure 14) ou le rayon atomique (Figure 15), suit particulièrement bien une évolution périodique au niveau des familles considérées.

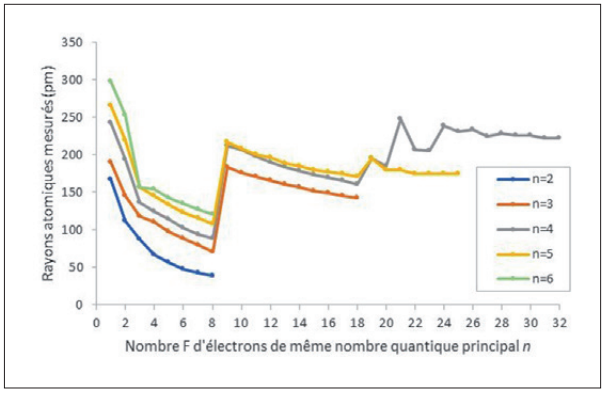

Figure 15. Rayons atomiques mesurés en fonction de F

Considérons à présent l'évolution de l'affinité électronique lorsque le nombre d'électrons de même nombre quantique principal *n* croît (Figure 16). Ici, on voit bien la difficulté pour attacher un électron supplémentaire (il faut plus d'énergie) lorsque le sous-niveau $\ell = 1$ se remplit car l'espace disponible près du noyau se réduit (orbitales p_x, p_y et p_z). La répulsion des électrons déjà présents semble similaire pour les *n* différents. C'est moins le cas pour le sous-niveau $\ell = 2$ car la présence moyenne de l'électron supplémentaire est située plus loin du noyau et donc l'espace disponible est plus important ($dV = 4\pi r^2 dr$).

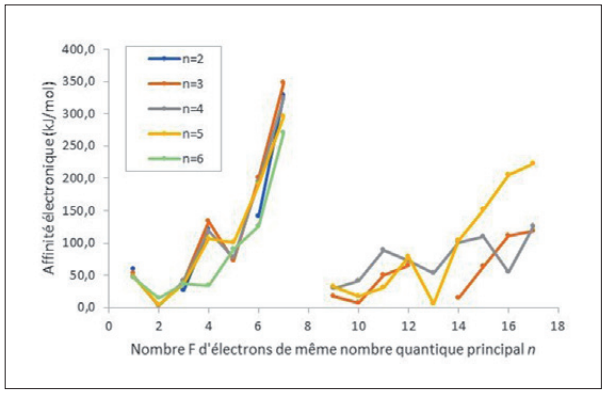

Figure 16. Affinités électroniques en fonction de F

Plus étonnant encore, cette similitude apparaît aussi pour l'énergie de formation de certain composés oxygénés binaires X_xO_y classée par rapport au paramètre F de l'atome X (Figure 17). Le tableau 2 qui donne les composés utilisés, est tiré de la figure 6-4 du remarquable ouvrage de R.T. Sanderson [7]. D'autres similitudes de propriétés (conductibilité thermique, enthalpie d'ébullition des composés oxygénés binaires, propriétés d'autres composés binaires avec le Br, le Cl,…) peuvent être également montrées.

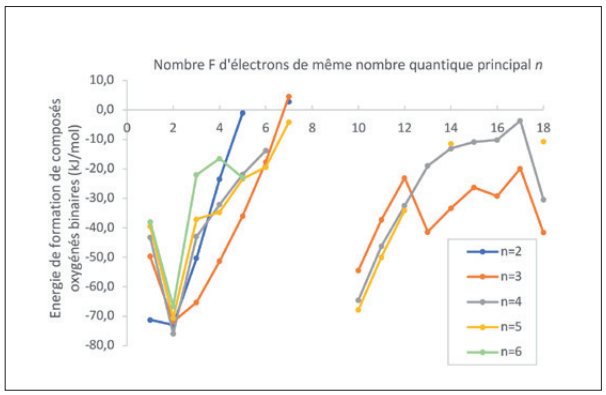

Figure 17. Energies de formation de certains composés oxygénés binaires à 25°C en fonction de F

De l'examen de toutes ces figures, on voit que pour un même F, les différents atomes ont des propriétés dont les valeurs sont très voisines. La notion de famille en découle de façon évidente et justifie le nom du paramètre. Remarquons le

F=	1	2	3	4	5	6	7	8	9	10	11	12	13	14	15	16	17	18
n=1	X_2O																	
2		XO	X_2O_3	XO_2	N_2O_5	XO_2	OF_2											
3					P_4O_{10}		Cl_2O_7			XO_2	X_2O_5	CrO_3	Mn_3O_4	Fe_3O_4	CoO_4	NiO	CoO_4	XO
4					As_2O_5		-					MoO_2	Tc_2O_7	RuO_2	RhO	PdO	AgO_2	
5					Sb_2O_5		I_2O_5					WO_2	-	OsO_4	-	-	-	
6					Bi_2O_3		-											

Tableau 2. Les composés oxygénés binaires utilisés pour la figure 17

rôle capital des électrons du niveau d'énergie occupé le plus élevé, électrons qui se trouvent généralement le plus souvent dans la périphérie de l'atome et qui correspondent à des électrons de valence.

4. Les configurations électroniques

La recherche des configurations électroniques est simplifiée en reprenant au bas des colonnes le nombre d'électrons du sous-niveau d'énergie le plus élevé de l'état fondamental, sous-niveau qui se remplit ; les autres, d'énergie inférieure, sont normalement complets. La configuration électronique (limitée au nombre quantique principal et orbital) du dernier électron ajouté est très simplement retrouvée par la position : toutes les cases supérieures à la position de la case de l'atome sont remplies et le nombre au bas de la colonne de la case donne le nombre d'électrons sur le sous-niveau. L'indication $10s^1$ au bas de la colonne 17 permet de tenir compte du gain d'énergie de la configuration de niveau complet avec un seul électron s par rapport à la situation « régulière » avec un niveau incomplet de 9 électrons pour tout le groupe 17.

Il n'est plus nécessaire de recourir à un tableau séparé des configurations. Ainsi le n et ℓ de l'électron ajouté sont déterminés facilement. Plus besoin d'introduire des règles *ad hoc* ou mnémotechniques pour retrouver ces nombres. On suit la progression en Z vers la droite ou vers le bas. Par ex., la structure du Fe est composée des électrons de nombres quantiques n = 1 et n = 2, ceux avec n = 3, ℓ = 0 ou 1, ceux avec n =4, ℓ = 0 et enfin six (au bas de la colonne) électrons avec n = 3 et ℓ = 2. En notation spectroscopique, on a pour le Fe :

$$1s^2\ 2s^2\ 2p^6\quad 3s^2\ 3p^6\quad 4s^2\quad 3d^6\quad \text{ou}\quad (Ar)\ 4s^2\ 3d^6$$

Les blocs s et p n'ont pas d'exception. Une seule exception avec n = 3 et ℓ = 2 (Cr) et cinq avec n = 4 et ℓ = 2 (Nb, Mo, Rn, Ph, Pd) ; les autres sont dans les lanthanides et actinides. Les quelques exceptions à cette procédure peuvent figurer explicitement dans la case. Dans la case du Mo par ex., on observe la configuration :

$$(Kr)\ 5s\ 4d^5\quad \text{au lieu de}\ (Kr)\ 5s^2\ 4d^4\quad \text{attendu.}$$

5. Bénéfices

Par rapport au tableau usuel, la nouvelle représentation a de nombreux avantages :

- Les éléments suivent un ordre logique en Z sans exception.
- Les nombres d'éléments par période sont bien retrouvés (2 8 8 18 18 32 32) conformément au principe Real Aufbau de la chimie quantique relativiste.
- Les atomes des groupes principaux s et p sont rassemblés.
- L'usage systématique des couleurs pour le fond des cases permet de faire ressortir les comportements chimiques. Ainsi, la place de l'He n'est plus problématique et le comportement multiple de l'H est suggéré.

- La distribution claire des sous-niveaux remplis et ceux qui se remplissent permet de retrouver facilement les configurations électroniques en n et ℓ avec seulement quelques exceptions qui seront écrites explicitement dans le nouveau TP.
- L'allure générale du tableau est très proche de celle du tableau usuel (Figure 18) et conserve les habitudes des praticiens de la chimie.

Grâce à ce tableau (Figure 6), on constate que le facteur d'ordonnancement dans les périodes est le nombre F d'électrons sur le niveau occupé de n le plus élevé (paramètre de famille). Il est aisé de trouver sur quel niveau l'électron ajouté à l'élément précédent va se situer pour tous les éléments importants des blocs s, p et même d (niveaux n = 1, n = 2 et n = 3).

Pour la question de la position de l'hélium, il est situé au sommet de la colonne 2 car c'est sa place ! Sa configuration électronique complète comporte deux électrons et non huit. Sa nature chimique différente, liée au premier niveau d'énergie complet, est clairement indiquée par le fond coloré de la case (Figure 6). L'usage systématique des couleurs pour le fond des cases permet de faire ressortir les comportements chimiques.

6. Conclusions

Le tableau usuel a son origine il y a 150 ans et depuis lors, les progrès de la compréhension de la structure électronique ont été considérables. L'apport relativiste de la Chimie Quantique récente change un peu les niveaux d'énergie dans l'atome. Dans un tableau, le placement des cases sur les sous-niveaux selon la hiérarchie énergétique permet d'obtenir une progression en Z cohérente et d'omettre l'idée fausse des couches K, L, M,... (au lieu de niveaux). Il ne sera pas nécessaire d'utiliser la règle d'édification ($n + \ell$) non justifiée et de l'abandonner par la suite. Il en résulte un tableau logique, beaucoup plus facile à assimiler et à utiliser. L'introduction d'un nouveau paramètre dit de famille permet de montrer les similitudes très nombreuses et même insoupçonnées, indicatrices de la périodicité chimique.

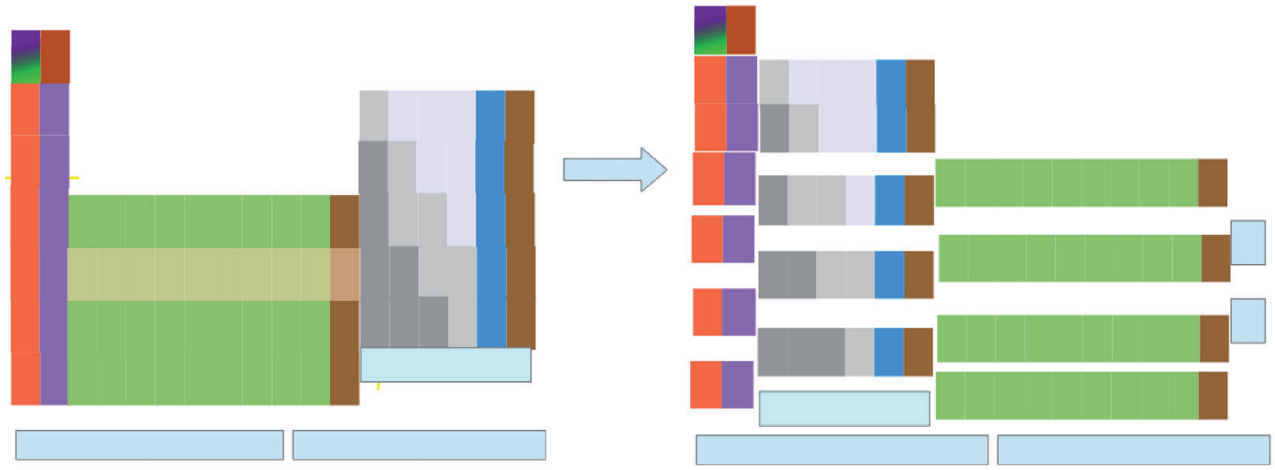

Figure 18. Allures générales de l'ancien et du nouveau tableau

Remerciements

Que le réviseur anonyme reçoive ici toute l'expression de ma gratitude pour l'aide importante qu'il m'a apportée. Tous mes remerciements à Benoît Champagne, Bernard Mahieu, Brigitte Van Tiggelen, Xavier Urbain et Koen Stegen pour leur encouragement et les nombreuses remarques et discussions constructives ainsi qu'aux deux étudiants de l'UNamur (Clémence Coquillart et Maxime Mathieu) pour l'aide à la préparation des versions finales des figures.

Annexe

Le paramètre de famille permet une jolie illustration inattendue du modèle de Bohr. Considérons les énergies d'ionisation des premiers éléments (au moins jusque Z = 32) normalisées par rapport à l'énergie d'ionisation de l'hydrogène. Les racines carrées de ces énergies sont portées en graphique en fonction de Z avec l'ordonnancement par le paramètre de famille. Dans la Figure 19, la première suite 1 concerne, en commençant par le bas, les énergies d'ionisation de H, He^{+}, Li^{++}, Be^{3+},... et ainsi de suite c'est-à-dire les ions avec un seul électron F = 1 ; la suite 2 implique F = 2 (He, Li^{+}, Be^{2+}, B^{3+}, C^{4+},…). La suite 3, celle des ions avec 3 électrons etc. La pente des droites est proportionnelle à 1/n en accord avec la théorie de Bohr ($E/E_H=Z^2/n^2$) avec *n* le nombre quantique principal correspondant au nombre F de l'atome ou de l'ion.

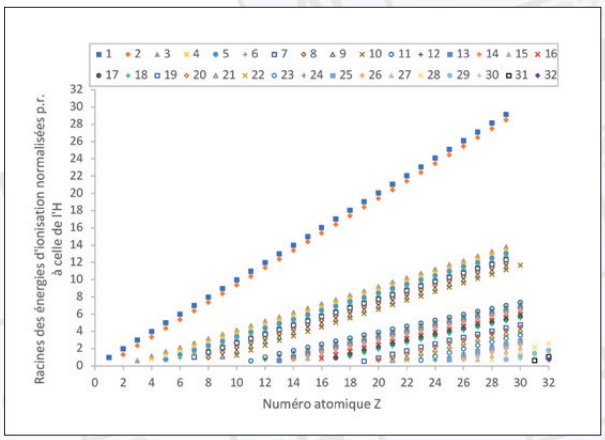

Figure 19. Racines carrées des énergies d'ionisation normalisées en fonction de Z. La couleur indique la valeur de F

Références

[1] C. Janet, http://www.meta-synthesis.com ® Web Book ® the INTERNET database of PT 1928 Janet and 2014 Jodogne's Janet PT 2e et puis 14e

[2] E.G. Mazurs. Graphic Representation of the Periodic Table during one hundred years, **1975**, Univ. Alabama Press, Alabama USA p96.

[3] M. Dolg, X. Cao, Chem. Rev. *Quantum Chemistry Issue* **2012**, *112*, 403-480

[4] H. Nakatsuji, Acc. Chem. Res. **2012**, 45, 1480-1490

[5] P. Pyykkö, Chem. Rev., *Quantum Chemistry Issue* **2012**, *112*, 371-384

[6] E.R. Scerri, Int. J. Quantum Chem. **2009**, *109*, 959-971

[7] R.T. Sanderson, Chemical Periodicity, Reinhold N.Y. **1975,** 112

Wendy H. MÜLLER
F.R.S.-FNRS Research Fellow
PhD thesis supervised by Prof. Gauthier EPPE
Mass Spectrometry Laboratory, MolSys Research Unit, Chemistry Department
University of Liège, Allée du Six Août 11, B6c Sart-Tilman,
4000 Liège (Belgium)
wmuller@uliege.be, +32 (0)4 366 3567

A molecular imaging approach combining Raman Spectroscopy and Mass Spectrometry to study biological samples

Abstract
The study of biological samples, like biological tissues or microbial communities, can be very complicated as such kind of samples are in essence extremely complex. This complexity is mainly expressed by the heterogeneity of their molecular microstructure, both in terms of spatial arrangement and chemical composition. Thus, the analysis of biological samples requires analytical techniques able to visualise the distribution of the chemical compounds within the sample at a molecular level and with a high spatial resolution. To this end, the use of molecular imaging techniques is a promising avenue and, in particular, the development of multimodal approaches (that is, combining several complementary techniques to overcome the limitations of the individual ones) has grown interest in the last decade. Here, we show that the combination of Raman spectroscopy and mass spectrometry imaging represents an up-and-coming implementation of multimodal molecular imaging for the study of complex biological samples.

Keywords
Raman Spectroscopy, SERS, Mass Spectrometry, SALDI-MS, Imaging

1. Introduction

Biological samples, such as biological tissues, cells or microbial communities are complicated molecular systems. Indeed, their heterogeneous molecular microstructure turns out to be both chemically and spatially complex. Yet, the investigation of the chemical composition of biological samples, at the molecular level and with spatial information, is of particular interest in various fields. Indeed, visualising the spatial molecular distributions in cells and tissues and associating them with structural or other biochemical features can, for example, give some insights into the biological mechanisms involved in the development of a disease [1], facilitate clinical diagnosis by identifying the regions of pathology [2,3] or enable the engineering of novel biotechnological applications.

Conventional imaging techniques include histology, immunohistochemistry [4] and fluorescence microscopy, which allow the visualisation of the distribution of targeted molecules within the biological samples. Histology and histochemistry are the standard methods, routinely applied to reveal general tissue morphology, cell type, subcellular structure and the presence of endogenous substances that react

with the stains [1]. However, these approaches are only qualitative. Fluorescence microscopy using dyes or quantum dots has also been extensively used to study biochemical processes, especially at the single cell level, as it provides high sensitivity and high contrast images. However, most fluorescent dyes exhibit photobleaching and photodegradation [5] and the band width of fluorescence peaks are usually broad [5], limiting the multiplex detection (i.e. detection of multiple analytes simultaneously). Moreover, both histological and fluorescence approaches lack of specificity at the molecular level [1,6].

1.1. Emergence of molecular imaging techniques

Nowadays, molecular imaging techniques have emerged as a powerful implementation of molecular analytical techniques to investigate and visualise the complex heterogeneity of the chemical composition of various samples [7-10]. To this end, the sample is analysed by a molecular analytical technique able to record the chemical information at different spatial locations (Figure 1). For example, mass spectrometry and vibrational spectroscopy imaging techniques are particularly well adapted to study biological samples. With these techniques, the biological sample is interrogated by a laser that moves along the x and y axes. A spectrum (either a Raman spectrum or a mass spectrum) is obtained at each (x,y) location. Then, the molecular image (also called *2D cartography*) revealing the distribution of the analytes within the sample is reconstructed through data processing (Figure 1). Finally, the reconstructed images allow the identification of structures and the visualisation of molecular changes occurring in precisely defined regions of the sample. This includes the evaluation of the spatial distribution of metabolites produced, for example, during intercellular communication.

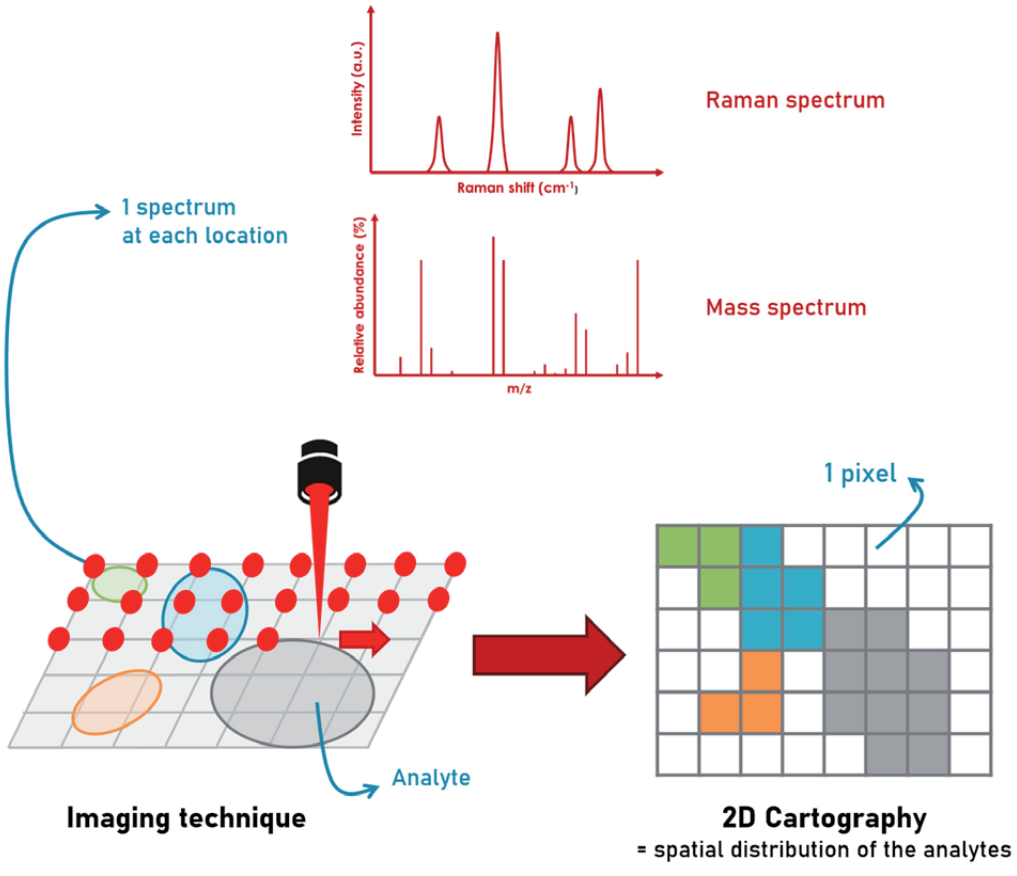

Figure 1: Schematic representation of a molecular imaging approach

2. Molecular analytical techniques to image biological samples

The investigation of the spatial molecular microstructure of biological samples is still a challenge as it requires advanced analytical techniques able to visualise the distribution of the molecular components with both high specificity and high spatial resolution. Multiple imaging modalities can be used depending on the sample and on the desired information [3]. The selection of the most appropriate imaging technique for the sample analysis is not straightforward and depends on several factors such as the required spatial resolution, the levels of sensitivity and specificity, the need for dynamic or *in vivo* information or the need for quantitative information [3]. However, each imaging technique has its own advantages and limitations, therefore a compromise will generally have to be made in order to meet as many criteria as possible. As previously said, there are numerous imaging techniques that can be employed to study biological samples. However, this article will only be focused on Raman Spectroscopy and Mass Spectrometry, which are two complementary techniques commonly used in our laboratory to image biological samples.

2.1. Achieving high spatial resolution with Raman Spectroscopy Imaging

Raman spectroscopy, based on the principle of Raman scattering (inelastic light scattering), is a rapid, non-targeted and non-destructive [11-14] quantitative and qualitative vibrational molecular spectroscopy technique used for the characterisation of either organic or inorganic compounds [8, 15, 16]. During the analysis, a monochromatic light is sent to the sample and the Raman scattered light is then collected and analysed. Raman scattered photons display a shift in frequency, called the *Raman shift*, compared to the frequency of the excitation light [3]. A conventional Raman spectrum (Figure 2) represents the Raman shift on the horizontal axis and the intensity on the vertical axis. In other words, the molecular vibration information can be read on the horizontal axis while the strength of the activity (intensity) can be read on the vertical axis [17].

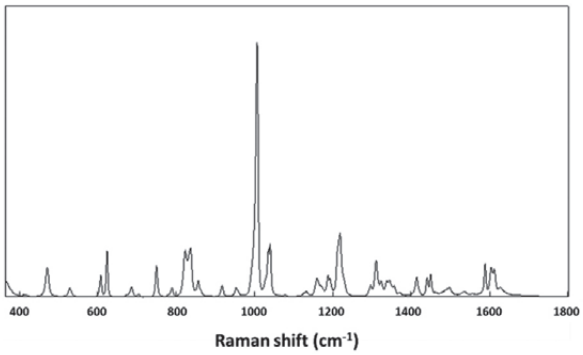

Figure 2: Raman spectrum of Phenylalanine (laser line = 532 nm)

Every molecule has its own unique vibrational signature. Therefore, Raman Spectroscopy can be used to simultaneously detect and identify various molecules within the same area (by deconvoluting or decomposing the complete Raman spectrum into pure components using advanced statistical data treatments) [3].

Raman spectroscopy can also be coupled to optical devices such as microscopes, allowing the imaging of different samples [18] by localising the signals originating from molecular functions, as shown in Figure 3 and Figure 4.

A great advantage of Raman Spectroscopy Imaging is that this technique does not require any specific sample preparation. However, in the case of biological samples, cryosectionning may be necessary to expose the internal section to be imaged. After cryosectionning, sample sections are mounted on a microscopic slide and placed under the Raman microscope to perform the analysis. Some biological samples such as cell cultures in a Petri dish can also be analysed as they are. Sensitive samples might require a chemical fixation step, for conservation purposes, prior to the Raman analysis.

The undeniable strength of this imaging technique lies in the spatial resolution that can be achieved [19] (down to a few hundreds of nanometres), which is requested for the interrogation of biological samples (e.g. mouse brain sections [12, 20]). Spatial resolution in

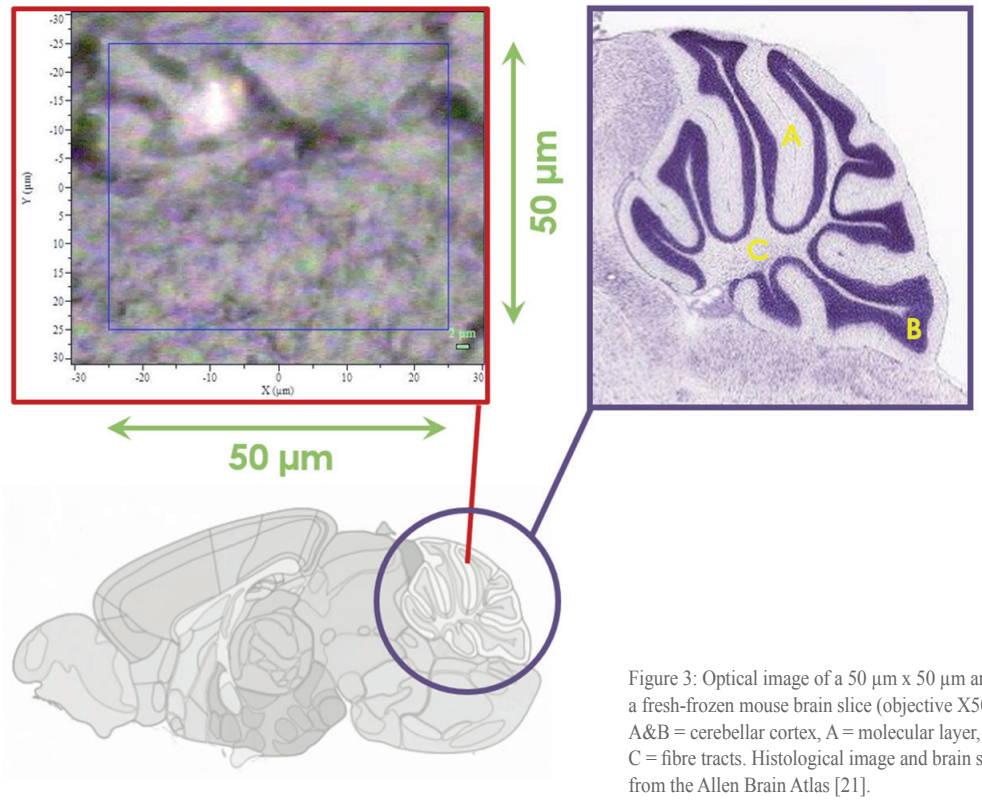

Figure 3: Optical image of a 50 µm x 50 µm area within a fresh-frozen mouse brain slice (objective X50), A&B = cerebellar cortex, A = molecular layer, B = granular layer, C = fibre tracts. Histological image and brain scheme coming from the Allen Brain Atlas [21].

Raman Spectroscopy Imaging is actually only limited by the diffraction limit:

$$R = \frac{1.22\lambda}{2n \sin\theta} = \frac{1.22\lambda}{2NA}$$

With R, the spatial resolution at the limit of diffraction;
λ, the illumination wavelength;
n, the medium refractive index;
θ, half of the angular aperture;
NA, the numerical aperture of the objective.

Because of the relatively short wavelengths used in Raman spectroscopy (UV, visible and near Infrared range of wavelengths) and thanks to the refractive objectives used in Raman Spectroscopy Imaging, micron-scale spatial resolution can be achieved.

Consequently, Raman cartographies can focus on very small regions of interest with a high spatial resolution. As an example, imaging of a 50 µm x 50 µm area of the cerebellum of a mouse brain (Figure 3) was performed by Raman spectroscopy with a spatial resolution of 4 µm.
An important part of imaging analyses is the data processing. Indeed, a significant number of spectra is obtained during the imaging run. It is generally impossible to detect the differences, sometimes subtle, between all recorded spectra without the implementation of advanced statistical data treatment methods. For instance, the 144 pre-processed Raman spectra, recorded in the 50 µm x 50 µm area of the mouse cerebellum, are shown in Figure 4.

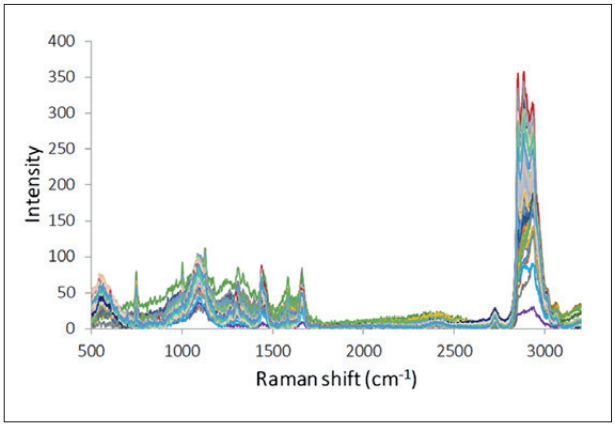

Figure 4: Pre-processed spectra obtained during the imaging of the mouse brain 50 x 50 µm cartography.

In order to identify compounds of interest in the different regions of the cerebellum, Multivariate

Curve Resolution – Alternating Least Squares (MCR-ALS) was used. In a spectroscopic context, MCR-ALS is a data processing method aiming at recovering concentration profiles and "pure" spectra of the corresponding components from an unresolved mixture and therefore, to decompose the signal of the original data into pure individual components. Indeed, MCR-ALS decomposes the complex spectrum in each pixel of an image into a linear combination of pure components spectra (weighted according to their concentration in each pixel). MCR-ALS optimises spectra and concentrations matrices of the pure components of the unresolved mixture under certain constraints. Constraints are criteria of (bio)chemical or mathematical origin that the calculated profiles must fulfil. For example, "non-negativity" constraint has to be applied as both concentrations and band intensity in vibrational spectroscopy cannot be negative.

An MCR-ALS analysis was performed on the dataset comprising all the pre-processed Raman spectra of the mouse cerebellum area. A 3-components model was chosen as, in that case, 3 components are sufficient to explain 99.6% of the total variability of the system. The three pure components spectra are shown on Figure 5 and images of these pure components distribution within the cartography area are shown in Figure 6.

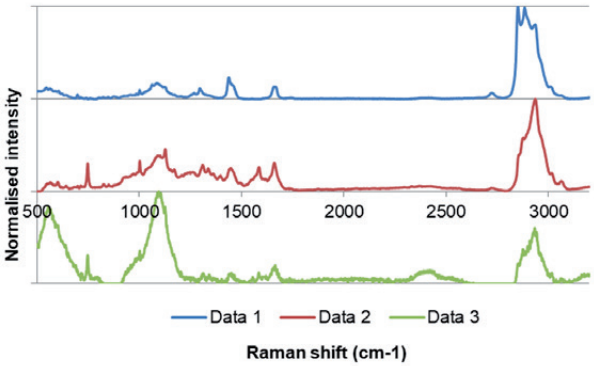

Figure 5: Pure components spectra calculated by MCR-ALS

Assignation of the peaks of the spectra generated by MCR-ALS (**Table 1**) was done and revealed that Data 3 mainly corresponds to the glass spectrum (of the microscopic slide that supports the mouse brain section) with the Raman bands at approximately 560 cm^{-1} and 1100 cm^{-1}, which is why the intensity of this spectrum seems homogeneous within the entire image area (Figure 6). Data 1 is mainly related to lipids. Indeed, the peaks that are only found in the Data 1 spectrum are mainly specific to lipids. On the other hand, Data 2 specific bands indicate an area rich in proteins and nucleic acids and also lipids, which are abundant in the brain.

DATA	Peak value (cm^{-1})	Examples of possible assignment
DATA 1	2884	CH_2 symmetric stretch of lipids, CH_2 asymmetric and CH stretches of lipids and proteins
	2851	CH_2 and CH_3 symmetric stretch of lipids, CH_2 asymmetric stretch of lipids and proteins
	1297	Methylene twisting, fatty acids, CH_2 deformation (lipids), $-(CH_2)_n-$ in-plane twist vibration (lipid band)
	546	Cholesterol
DATA 2	1585	Phenylalanine C=C bending mode, C=C olefinic stretch (protein assignment), hydroxyproline
	1361	Tryptophan, guanine
	1172	Tyrosine (protein assignment), (CH) phenylalanine and tyrosine, cytosine, guanine
	748	Thymine (ring breathing mode of DNA/RNA bases), DNA, symmetric breathing of tryptophan (protein assignment)
DATA 3	560	Glass
	1100	Glass

Table 1: Examples of peak assignations of Data 1, 2 and 3 based on widely peak frequencies and assignments of biological tissues [22]

This corroborates with the histological analysis of the tissue since Data 1 corresponds to the white matter rich in myelinated axons and thus rich in lipids, whereas Data 2 corresponds to the grey matter, rich in cell bodies

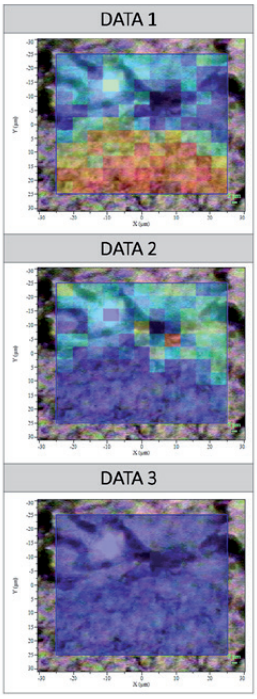

Figure 6: MCR-ALS images showing the distribution of pure components within the area

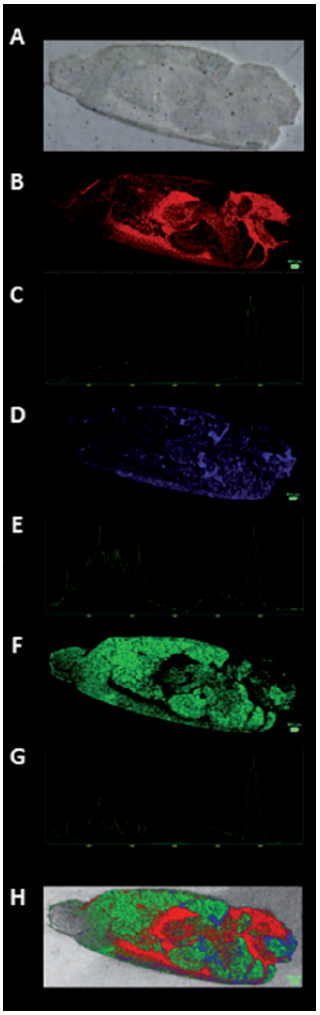

Figure7: A-Optical image of a mouse brain section; B, D, F-Raman image of pure components; C, E, G- Raman spectra of pure components; H-Superposition of the three Raman images (C, E & G)

Biological sections can also be imaged on their entire surface. As an example, entire mouse brain sections were interrogated by Raman Spectroscopy Imaging as shown in Figure 7.

As a non-destructive and non-invasive technique, Raman Spectroscopy Imaging can also be performed *in vivo* [14].

However, while Raman spectroscopy does not suffer from water interference, it is deeply impacted by the strong fluorescence signals often emitted by biomolecules or impurities of the sample, which can hide the Raman signals, preventing the acquisition of an interpretable spectrum [23], as shown in **Figure 8** in the context of bacteria analysis.

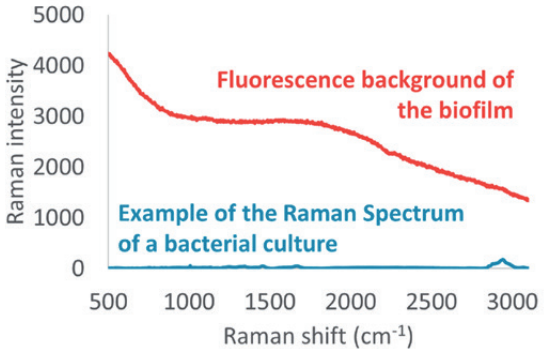

Figure 8: Fluorescence background during acquisition of a Raman spectrum of a bacterial biofilm

Moreover, when light interacts with matter, the Raman scattering is the minor process. Indeed, most photons are elastically scattered (Rayleigh scattering), while only one Raman photon is scattered for 10^6 – 10^8 Rayleigh photons [3, 24]. Therefore, Raman spectroscopy also suffer from poor sensitivity [19].

2.2. Surface-Enhanced Raman Spectroscopy to improve the sensitivity

However, these drawbacks of Raman spectroscopy (i.e. poor sensitivity and autofluorescence of the samples) can be overcome by the deposition of metallic nanoparticles on the sample surface. Indeed, in this approach, called *Surface-Enhanced Raman Spectroscopy* (SERS), the Raman effect is amplified by 6 to 10 orders of magnitude [25-28] due to the presence of the nanoparticle metallic surface onto which the Raman active molecules are adsorbed (Figure 9).

In opposition to classical Raman Spectroscopy Imaging that necessitates no specific sample preparation, SERS imaging requires the deposition of nanoparticles on the sample surface. To this end, the nanoparticles are suspended in a polar solvent (e.g. water, acetonitrile, methanol, ethanol or a mixture of some of these solvents) and then spayed onto the sample surface. In our laboratory, the deposition is performed using an automated spotting device, initially developed for the deposition of MALDI matrices, for Mass Spectrometry Imaging, *see MALDI-MS section*)

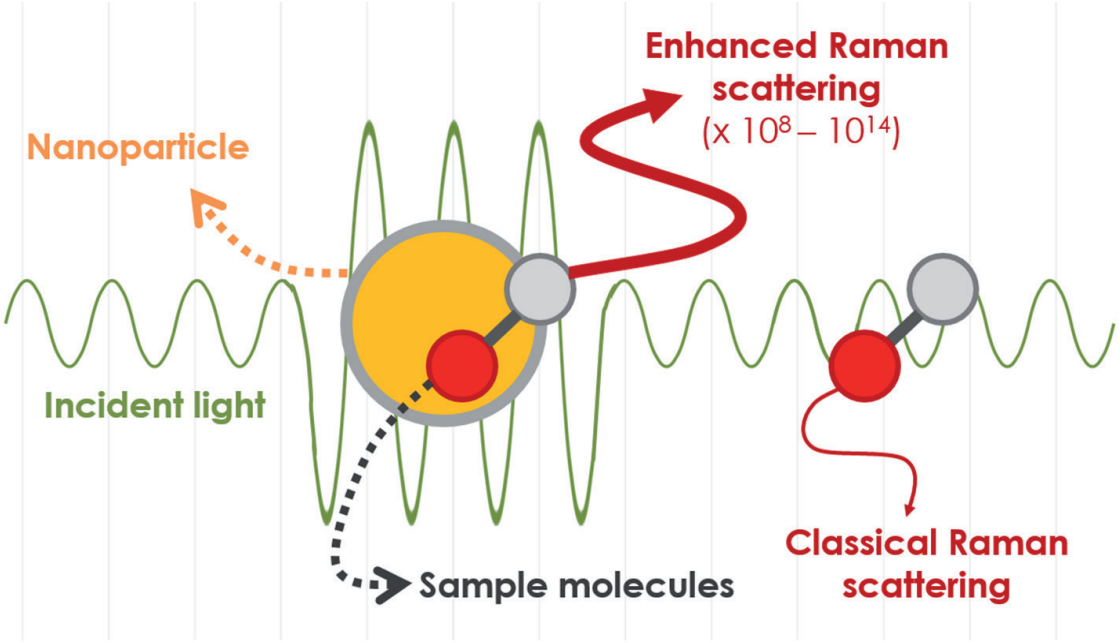

Figure 9: Schematic representation of Surface-Enhanced Raman Scattering

that is equipped with a capillary spray head ensuring the deposition of a homogeneous film of nanoparticles suspension over the sample.
SERS is also based on the principle of Raman scattering and has therefore the same overall advantages and limitations as "classical" Raman spectroscopy. The main difference obviously lies in the signal exaltation in SERS, giving this technique much more sensitivity than "classical" Raman spectroscopy, what can lead to faster image acquisition [19].

The exact mechanisms behind the signal exaltation in SERS are still not fully understood. However, two exaltation paths are generally accepted in the literature: the electromagnetic exaltation and the chemical exaltation [24, 29, 30]. Briefly, the electromagnetic exaltation mechanism contributes to the strongest signal amplification (factor 10^4 - 10^7) [29, 31] and is due to the excitation of the surface plasmon (shown in Figure 9), which corresponds to a collective oscillation of the conduction electrons of the metal nanostructure [30]. Under certain irradiation conditions, the surface plasmon is activated by the incident electromagnetic radiation (resonant interaction), which increases the electromagnetic field intensity at the close vicinity of the surface of the nanoparticle [29, 32]. In turn, the interaction between this amplified electromagnetic field and the adsorbed Raman active molecule increases the intensity of the Raman scattering [32]. On the other hand, the chemical exaltation only contributing to a signal amplification by a factor 10^2 has been introduced to explain why different molecules have different exaltation factors in identical experimental conditions [29, 30]. However, this exaltation mechanism is still subject to controversy. Different theories try to explain this exaltation in which the Raman active molecule, chemically adsorbed on a metal, has new resonance "paths". These resonance paths can be created by the formation of a complex between the molecule and the metal or by the creation of charge transfer complexes between the molecule and the metal [33].

Moreover, metal nanoparticles can quench autofluorescence that is common with biological samples [19, 34].

However, SERS has specific limitations: the signal intensity is not necessarily directly proportional to the concentration of the analytes [35] and suffers from poor reproducibility [19]. Indeed, the signal strongly depends on the nanometric substrate (influence of size, shape and chemical nature, for example) [29]. Moreover, while Raman spectroscopy is considered as a non-destructive

technique, the application of nanoparticles to the sample in SERS may be problematic if other analyses (e.g. histological analyses) need to be later performed on the same sample. *In vivo* applications of SERS are also limited as the potential toxicity of the nanoparticles is still not completely understood.

Unlike classical Raman spectroscopy, SERS imaging can be performed following two different approaches: non-targeted (similar to classical Raman spectroscopy with surface-enhanced signals) and targeted by the use of SERS nanoprobes (Figure 10). The SERS nanoprobes can be prepared from metallic nanoparticles, for example, functionalised with a Raman reporter (a molecule selected to give an intense Raman signal and enabling the detection of the nanoprobe) and a targeting agent, which can be a peptide or an antibody, for instance, specific to a biological receptor or a particular molecule to target in the sample [36].

This targeting SERS approach also allows multi-analyte analyses through the specific molecular spectral signature of different Raman reporters and the very small peak width of the Raman spectral bands (10 to 100 times narrower than fluorescence peaks) [37, 38], offering SERS promising multiplexing capabilities [3]. In addition, unlike fluorescence, dyes used in SERS are not subject to photobleaching [14, 27].

However, both Raman spectroscopy and SERS have relatively low chemical specificity as they only identify functional groups based on the bonds vibrations. Therefore, in complex biological samples, these techniques will not be able to assign band values to a specific molecule present in the sample.

2.3. MALDI-MS provides a high molecular specificity but suffers from limited spatial resolution

Compared to vibrational spectroscopy imaging techniques, Mass Spectrometry Imaging (MSI) allows the identification of specific ions based on their mass-to-charge ratios and enables their localisation within the biological samples, but with a lower spatial resolution.

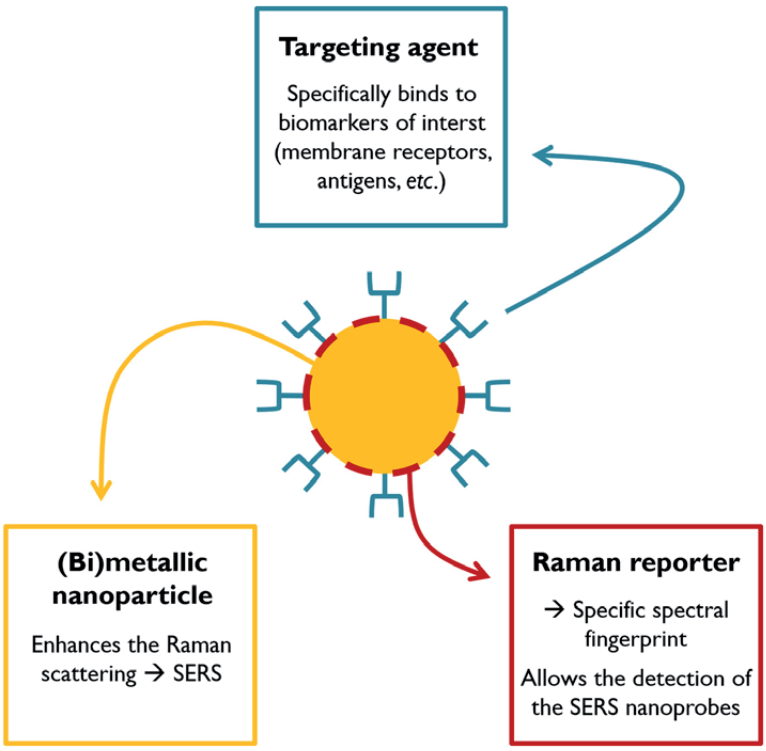

Figure 10: Schematic representation of a SERS nanoprobe

Among the range of ion sources used in mass spectrometry, the soft Matrix-Assisted Laser Desorption/Ionisation Mass Spectrometry (MALDI-MS), which involves a laser striking the sample co-crystallised with an organic matrix in order to promote desorption and ionisation of the analytes, has been extensively used for the imaging analysis of biological samples [10] (Figure 11).

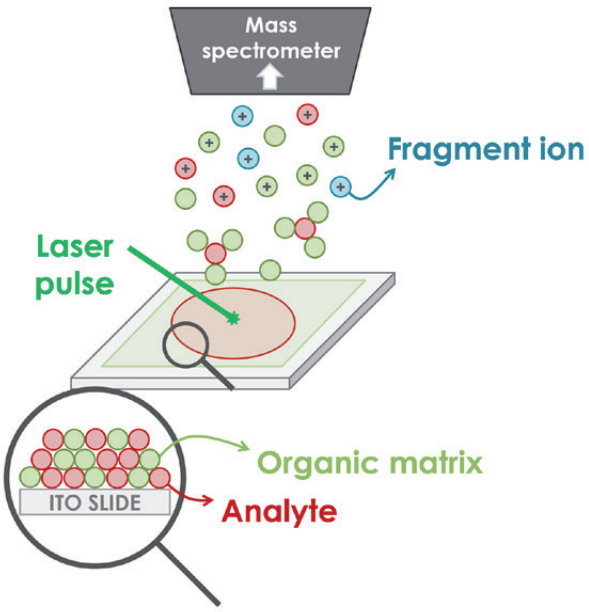

Figure 11: Schematic view of MALDI-MS process

Indeed, MALDI-MS allows the sensitive and rapid analysis of a wide range of compounds [39 - 41], mainly macromolecules (> 700 Da) [42, 43] such as proteins, peptides, lipids and bio-polymers [44] thanks to the formation of monocharged pseudomolecular species ($[M+H]^+$, $[M-H]^-$ and alkali cationised molecules) and limited fragmentation [41, 45]. Moreover, MALDI (and LDI ion sources, in general) are routinely coupled to high resolution mass spectrometry and provide access to the exact and accurate masses of the pseudomolecular ions produced at the surface of the sample [46], providing unambiguous identification of molecules.

Unfortunately, this technique has also several disadvantages, mainly due to the application of the organic matrix chosen to absorb the laser pulse and promote the charge transfer to the sample molecules.

Indeed, the matrix can contribute to ion suppression and spectral interferences in the low mass-to-charge range [2], which often prevents the detection of small molecules and metabolites especially in the range below 700 Da [40, 42, 44, 47-49]. In addition, the organic matrices are also characterised by a lack of reproducibility due to the inhomogeneous co-crystallisation with the analytes [44, 48]. The crystallisation of the matrix is also at the centre of another crucial issue regarding the spatial resolution. Indeed, the spatial resolution obtained with MALDI Mass Spectrometry Imaging (MALDI-MSI) is limited to a few tens of microns, corresponding to the size of the matrix crystals [49] (the crystal sizes of the commonly used 2,5-dihydroxybenzoic acid (DHB) and α-cyano-4-hydroxycinnaminic acid (CHCA) are generally comprised between 5 and 20 µm using spraying deposition) [49]. Such resolution prevents to extend the application of MALDI-MS imaging to cellular and subcellular analyses [49].

The sample preparation in MALDI-MSI is also more labour-intensive than in Raman Spectroscopy or SERS imaging). Indeed, the application of the organic matrix applied on the sample with the automated spotting device has to be done carefully in order to ensure an appropriate co-crystallisation of the analyte and the matrix. Moreover, the sample (bacterial culture, tissue sections, etc.) have to be mounted on a conductive support to allow the collection of the extracted ions towards the mass spectrometer.

2.4. From MALDI-MS to SALDI-MS to get around matrix-related issues

Here again, nanoparticles can be used to overcome the limitations of the “classical” well-known technique. Indeed, contrasting with MALDI-MS, Surface-Assisted Laser Desorption/Ionisation Mass Spectrometry (SALDI-MS) employs nanostructured substrates (that may be carbon-based, semiconducting or metallic) instead of organic matrices to promote desorption and ionisation [40] (Figure 12).

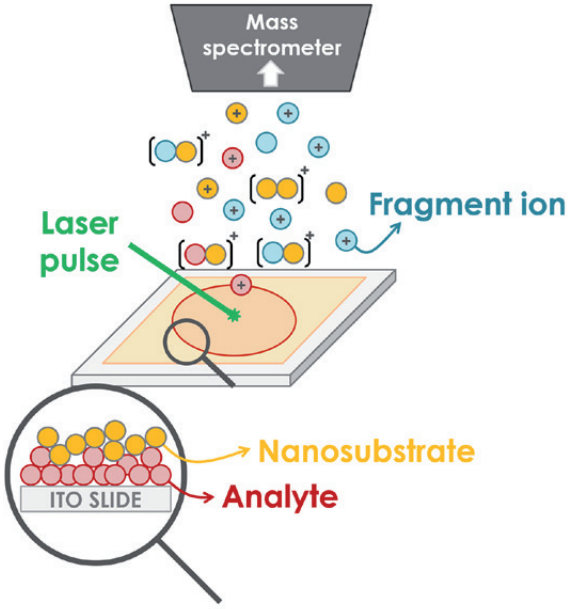

Figure 12: Schematic view of the SALDI-MS process

The SALDI nanosubstrates have the same overall role as the organic matrices: they must be able to absorb the energy of the laser radiation, transfer this energy to the analytes to promote their desorption and provide a source of ionisation [40, 41]. Also, like MALDI-MS, SALDI-MS can be coupled to high resolution mass spectrometry.

In fact, SALDI-MS represents an interesting alternative to MALDI-MS as the use of nanostructured substrates allows to get around the matrix-related issues encountered in MALDI-MS [41, 45].

First, SALDI-MS is particularly effective for the analysis of small molecules (< 1000 Da) with moderate interferences [49, 50], which makes its analysable m/z range complementary to the one of MALDI-MS.

The second interesting feature of SALDI Mass Spectrometry Imaging (SALDI-MSI) is that images can be recorded in both ion modes with the same nanosubstrates (as shown in Figure 14 and Figure 15), while the ion mode in MALDI-MS is generally determined by the choice of the organic matrix. To construct these SALDI images (also called *ion maps*), a peak of the SALDI-MSI mean spectrum (corresponding to a defined m/z value and therefore, to a specific ion) (Figure 13) is selected and the intensity of this peak in each pixel of the image is represented by a colour gradient to build the SALDI image. The ion map thus shows the distribution of a specific ion in the sample.

Finally, the deposition of nanostructured substrates (following the same procedure as in SERS imaging) instead of an organic matrix eliminates the formation of large matrix crystals, providing visually better images with increasing spatial resolution [49], as shown in Figure 16.

The lateral resolution in SALDI-MSI is indeed only limited by the ionisation laser spot size (which can go down to 5 µm) and not by the size of the SALDI substrates themselves (as they are nanometric in size) [49, 51].

However, although the improved performances obtained with nanostructured substrates in SALDI-MSI have been increasingly recognised, SALDI-MSI is not used as much as the traditional MALDI-MSI [49]. One reason that could explain this fact is that SALDI-MS involves a series of complicated processes [50, 52], not yet fully understood, which can, in addition, be affected by various physicochemical properties of the SALDI nanosubstrates [44, 50, 53, 54]. Until now, research in SALDI-MS has focused on the engineering of novel substrates with improved performances or on the development of advanced applications in various fields [44]. Only a few studies have focused on the fundamental aspects of the desorption and ionisation mechanisms of the SALDI processes, which is still a subject of much controversy within the SALDI research field.

2.5. Multimodal molecular imaging approaches

As we have just seen in the previous sections, each imaging technique has its own strengths and weaknesses. However, these different imaging modalities should not be seen as competitive as they provide distinct and complementary information about the interrogated samples.

Therefore, in order to maximise the molecular information and to overcome the limitations

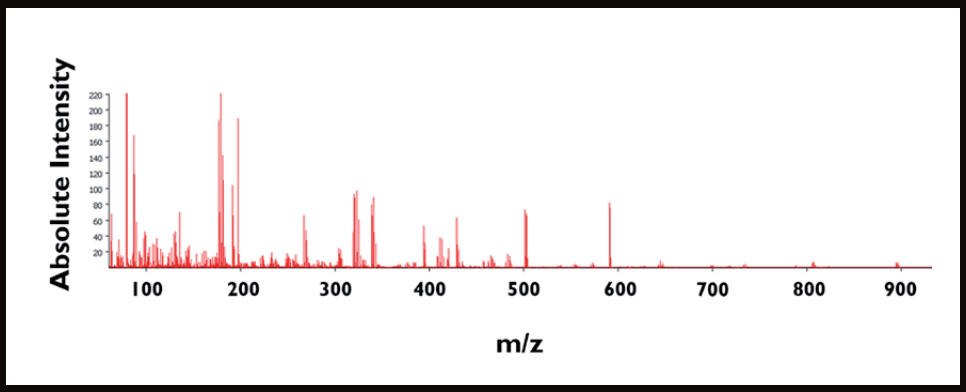

Figure 13: SALDI-MS mean spectrum of the imaging of a mouse brain section in negative ion mode

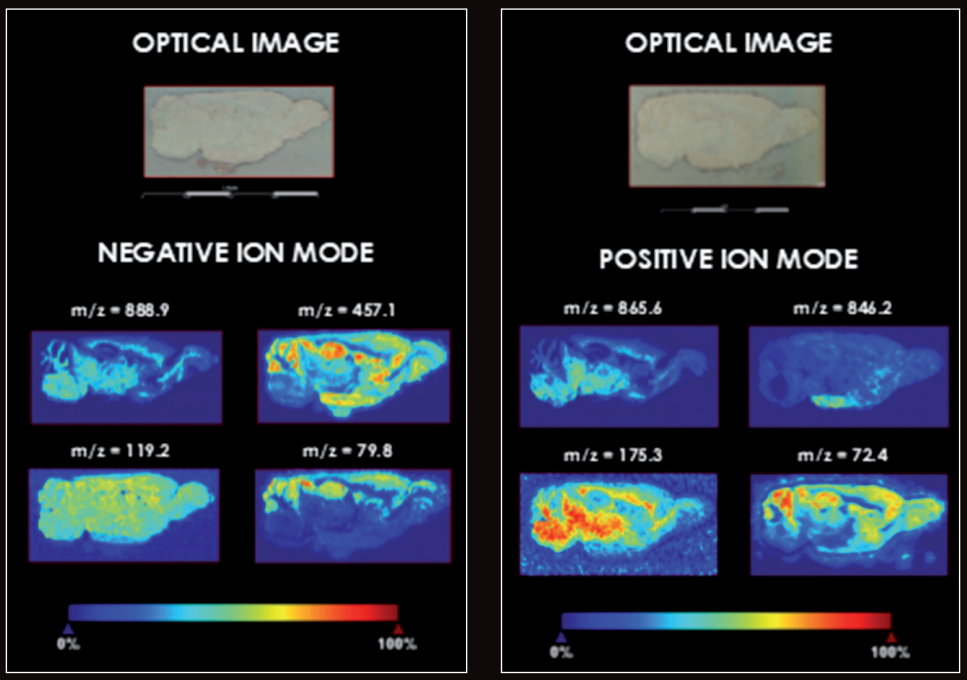

Figure 14: Some SALDI-MS images of the mouse brain section in negative ion mode using bimetallic core-shell gold@silver nanoparticles

Figure 15: Some SALDI-MS images of the mouse brain section in positive ion mode using bimetallic core-shell gold@silver nanoparticles

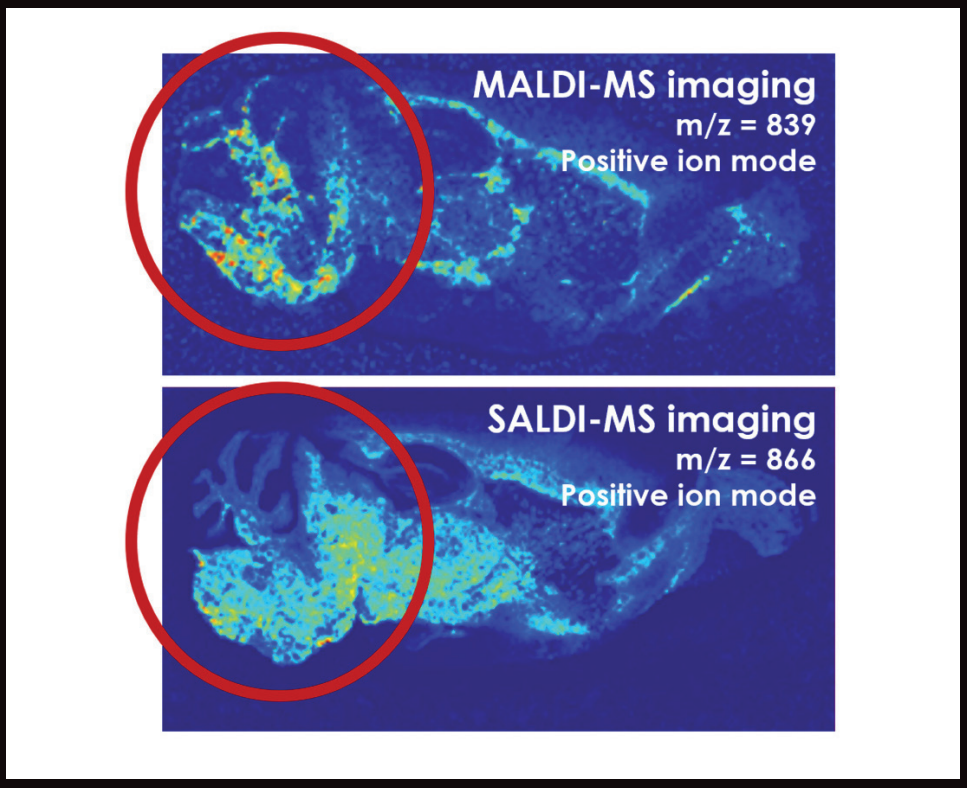

Figure 16: MALDI-MS and SALDI-MS imaging of a mouse brain section in positive ion mode, showing the increased image resolution in SALDI-MSI compared to MALDI-MSI, with the same laser spot size (i.e. 40 μm)

inherent to each individual technique used separately, several complementary imaging techniques can be combined in a multimodal approach.

A multimodal molecular imaging strategy involving both SERS and SALDI-MS imaging can be implemented on the same biological sample as they both use nanoparticles. This combination is particularly relevant as it benefits from the high spatial resolution of SERS and the high specificity of SALDI-MS imaging. SERS imaging, being a non-destructive technique, can be used upstream of SALDI-MS imaging.

However, if the combination of these two techniques into an integrated multimodal analytical strategy for molecular imaging looks easy on paper, in practice, it turns out to be challenging [19]. For instance, some challenges are inherent to the experimental preparation of the sample that has to be compatible with all the combined techniques [55]. Another challenge concerns the correlation of the molecular images independently obtained by different analytical methods, and thus with dissimilar spatial resolutions (in the (x,y) plane) but also different depths of penetration (z axis). Specific chemometrics statistical tools considering the specificity of all combined techniques as well as the spatial alignment of the images acquired on separate instruments must therefore be implemented [55].

3. Concluding remarks and future prospects

Molecular imaging has the great potential to highlight the spatial distribution of the molecular components in biological samples. It thus enables to reveal the heterogeneous molecular microstructure of tissues, to probe the metabolites excreted during intercellular interactions or to visualise the molecular changes occurring in specific regions of the sample, giving evidence of a pathology.

Various molecular imaging techniques have been developed in the last decades, each individual technique providing a particular molecular information such as the functional groups present in the molecules or the masses of these molecules distributed within the interrogated sample.

However, these molecular imaging techniques have their own strengths and weaknesses and thus, do not fulfil all the criteria required for an optimal imaging analysis when they are used separately.

That is why the development of multimodal molecular imaging approaches, combining several complementary techniques to overcome the limitations of the individual ones, has grown interest in the last decade. In particular, the combination of SERS and SALDI-MS imaging represents a promising avenue for the analysis of complex biological samples as it reveals the microstructure of the sample at the molecular level, with a high spatial resolution and high specificity.

Some challenges are undoubtedly inherent to the multimodal imaging approaches, such as the sample preparation that needs to be suitable with the combined techniques or the correlation of the molecular images independently obtained with different analytical modalities. Further analytical developments as well as advanced data processing methods are therefore required. Nevertheless, multimodal imaging has already evolved in recent years, opening new opportunities for the study of intricate biological samples. The combination of several molecular analytical techniques offers great potential to address the challenges faced in analytical chemistry applied to biology, biomedicine or biotechnology. We are thus convinced that multimodal molecular imaging approaches will continue to develop in the next five years as the information obtained from multimodal analyses can go beyond what we can learn from the analyses performed with individual techniques.

References

[1] Bishop, D. P.; Cole, N.; Zhang, T.; Doble, P. A.; Hare, D. J. *Chem. Soc. Rev.* **2018**, *47*, 3770-3787.

[2] Stopka, S. A.; Rong, C.; Korte, A. R.; Yadavilli, S.; Nazarian, J.; Razunguzwa, T. T.; Morris, N. J.; Vertes, A. *Angew. Chemie - Int. Ed.* **2016**, *55*, 4482–4486.

[3] James, M. L.; Gambhir, S. S. *Physiol. Rev.* **2012**, *92*, 897–965.

[4] Zhou, D.; Guo, S.; Zhang, M.; Liu, Y.; Chen, T.; Li, Z. *Anal. Chim. Acta* **2017**, *962*, 52–59.

[5] Zong, C.; Xu, M.; Xu, L.; Wei, T.; Ma, X.; Zheng, X.; Hu, R.; Ren, B. *Chem. Rev.* **2018**, *118*, 4946–4980.

[6] Giordano, S.; Morosi, L.; Veglianese, P.; Licandro, S. A.; Frapolli, R.; Zucchetti, M.; Cappelletti, G.; Falciola, L.; Pifferi, V.; Visentin, S.; D'Incalci M. ; Davoli E. ; *Sci. Rep*. **2016**, *6* (37027), 1–8.

[7] Addie, R. D.; Balluff, B.; Bovée, J. V. M. G.; Morreau, H.; McDonnell, L. A. *Anal. Chem.* **2015**, *87* (13), 6426–6433.

[8] Bocklitz, T. W.; Guo, S.; Ryabchykov, O.; Vogler, N.; Popp, J. *Anal. Chem.* **2016**, *88* (1), 133–151.

[9] Ozawa, T.; Yoshimura, H.; Kim, S. B. *Anal. Chem.* **2013**, *85* (2), 590–609.

[10] Sans, M.; Feider, C. L.; Eberlin, L. S. *Curr. Opin. Chem. Biol.* **2018**, *42*, 138–146.

[11] Chao, Y.; Zhang, T. *Anal. Bioanal. Chem.* **2012**, *404* (5), 1465–1475.

[12] Ivleva, N. P.; Kubryk, P.; Niessner, R. *Anal. Bioanal. Chem.* **2017**, *409* (18), 4353–4375.

[13] Ivleva, N. P.; Wagner, M.; Horn, H.; Niessner, R.; Haisch, C. *Anal. Bioanal. Chem.* **2009**, *393* (1), 197–206.

[14] Taylor, J.; Huefner, A.; Li, L.; Wingfield, J.; Mahajan, S. *Analyst* **2016**, *141*, 5037–5055.

[15] Ferraro, J. R.; Nakamoto, K.; Brown, C. W. "Chapter 2 - Instrumentation and Experimental Techniques" in "*Introductory Raman Spectroscopy*", Second Edition; Academic Press, San Diego, **2003**; pp 95–146.

[16] Enoch, S.; Bonod, N. in "*Plasmonics: From Basics to Advanced Topics*", Springer-Verlag, Berlin Heidelberg, **2012**.

[17] Nanophoton Corporation. Raman Spectroscopy, retrieved from www.nanophoton.net. (accessed Dec 4, 2019)

[18] Wang, Y.; Yan, B.; Chen, L. *Chem. Rev*. **2013**, *113* (3), 1391–1428.

[19] Masyuko, R.; Lanni, E. J.; Sweedler, V.; Bohn, P. W. *Analyst* **2013**, *138* (7), 1924–1939.

[20] Sandt, C.; Smith-Palmer, T.; Pink, J.; Brennan, L.; Pink, D. *J. Appl. Microbiol.* **2007**, *103* (5), 1808–1820.

[21] Allen Institute for Brain Science, Allen Brain Atlas, retrieved from mouse.brain-map.org (accessed Dec 4, 2019)

[22] Movasaghi, Z.; Rehman, S.; Rehman, I. U. *Applied Spectroscopy Reviews* **2007**, *42* (5), 493-541

[23] "Nanotechnology Characterization Tools for Biosensing and Medical Diagnosis"; Ed. Kumar, C. S. S. R., Springer-Verlag Berlin Heidelberg, **2018**.

[24] Tu, Q.; Chang, C. *Biol. Med.* **2012**, *8*, 545–558.

[25] Andreou, C.; Kishore, S. A.; Kircher, M. F. *J. Nucl. Med.* **2015**, *56* (9), 1295–1299.

[26] Jamieson, L. E.; Asiala, S. M.; Gracie, K.; Faulds, K.; Graham, D. *Annu. Rev. Anal. Chem.* **2017**, *10*, 415–437.

[27] Kneipp, J.; Kneipp, H.; Kneipp, K. *Chem. Soc. Rev.* **2008**, *37*, 1052–1060.

[28] Doering, W. E.; Piotti, M. E.; Natan, M. J.; Griffith Freeman, R. *Adv. Mater.* **2007**, *19*, 3100–3108.

[29] Haynes, C. L.; Mcfarland, A. D.; Duyne, R. P. Van. *Anal. Chem.* **2005**, *77* (17), 338–346.

[30] Prochazka, M. in "Surface-Enhanced Raman Spectroscopy - Bioanalytical, Biomolecular and Medical Applications"; Springer International Publishing Switzerland, **2016**.

[31] Dippel, B. Fundamentals & Technology of Raman Spectroscopy, retrieved from www.raman.de (accessed Dec 4, 2019).

[32] Lane, L. A.; Qian, X.; Nie, S. *Chem. Rev*. **2015**, *115*, 10489–10529.

[33] Moskovits, M. *Phys. Chem. Chem. Phys.* **2013**, 15, 5301–5311.

[34] Zheng, X.; Jahn, I. J.; Weber, K.; Cialla-May, D.; Popp, J. *Spectrochim. Acta Part A Mol. Biomol. Spectrosc.* **2018**, *197*, 56–77.

[35] Verdin, A. (Jul 27, **2017**) Optimisation de sondes SERS pour des applications bio-analytiques (master's thesis), Université de Liège, retrieved from MatheO.

[36] Fabris, L. *J. Opt.* **2015**, *17* (11), 114002.

[37] Vendrell, M.; Maiti, K. K.; Dhaliwal, K.; Chang, Y. *Trends Biotechnol.* **2013**, *31* (4), 249–257.

[38] Laing, S.; Gracie, K.; Faulds, K. *Chem. Soc. Rev.* **2016**, *45* (7), 1901–1918.

[39] Sekula, J.; Niziol, J.; Rode, W.; Ruman, T. *Analyst* **2015**, *140* (18), 6195–6209.

[40] Chiang, C.-K.; Chen, W.-T.; Chang, H.-T. *Chem. Soc. Rev.* **2011**, *40* (3), 1269–1281.

[41] Pilolli, R.; Palmisano, F.; Cioffi, N. *Anal. Bioanal. Chem.* **2012**, *402* (2), 601–623.

[42] Guinan, T.; Kirkbride, P.; Pigou, P. E.; Ronci, M.; Kobus, H.; Voelcker, N. H. *Mass Spectrom. Rev.* **2015**, *34*, 627–640.

[43] Altuntaş, E.; Schubert, U. S. *Anal. Chim. Acta* **2014**, *808*, 56–69.

[44] Picca, R. A.; Calvano, C. D.; Cioffi, N.; Palmisano, F. *Nanomaterials* **2017**, *7* (4), 75.

[45] Arakawa, R.; Kawasaki, H. *Anal. Sci.* **2010**, *26*, 1229–1240.

[46] Masyuko, R. N.; Lanni, E. J.; Driscoll, C. M.; Shrout, J. D.; Sweedler, J. V.; Bohn, P. W. *Analyst* **2014**, *139* (22), 5700–5708.

[47] Aminlashgari, N.; Hakkarainen, M. S *J. Am. Soc. Mass Spectrom.* **2012**, *23* (6), 1071–1076.

[48] Lim, A. Y.; Ma, J.; Chiang, Y.; Boey, F. *Adv. Mater.* **2012**, *24*, 4211–4216.

[49] Phan, N. T. N.; Mohammadi, A. S.; Pour, M. D.; Ewing, A. G. *Anal. Chem.* **2016**, *88*, 1734–1741.

[50] Song, K.; Cheng, Q. *Appl. Spectrosc. Rev.* **2019**, 1–23.

[51] Ho, Y.-N.; Shu, L.-J.; Yang, Y.-L. *Wiley Interdiscip. Rev. Syst. Biol. Med.* **2017**, *9* (5), e1387.

[52] Law, K. P.; Larkin, J. R. *Anal. Bioanal. Chem.* **2011**, *399* (8), 2597–2622.

[53] Lai, S. K.-M.; Cheng, Y.-H.; Tang, H.-W.; Ng, K.-M. *Phys. Chem. Chem. Phys*. **2017**, *19*, 20795–20807.

[54] Ng, K.; Chau, S.; Tang, H.; Wei, X.; Lau, K.; Ye, F. *J. Phys. Chem.* **2015**, *119*, 23708–23720.

[55] Ahlf, D. R.; Masyuko, R. N.; Hummon, A. B.; Bohn, P. W. *Analyst* **2014**, *139*, 4578–4585.

Pour vous faire membre de la SRC et accéder gratuitement à la revue Chimie Nouvelle :

il vous suffit de verser au compte BNP Paribas Fortis : BE60 2100 4208 0470
la somme indiquée dans le tableau ci-dessous :

Membres résidant en Belgique et au Luxembourg
Membres effectifs : **50 euros**
- participation gratuite ou à prix réduit à toutes les activités de la SRC
- abonnement gratuit à la revue "Chimie Nouvelle"
- accès gratuit à la bibliothèque de la SRC.

Membres associés : **25 euros**
- réservé, avec les mêmes avantages que les membres effectifs, aux jeunes diplômés du deuxième cycle pendant deux ans, aux professeurs de l'enseignement secondaire et aux retraités.

Membres Juniors : Gratuit
- réservé aux étudiants de dernière année du 2e cycle universitaire (2e master), des Ecoles d'Ingénieurs industriels et des graduats en Chimie et Biochimie avec les mêmes avantages que les membres effectifs.

Demandeurs d'emploi : **15 euros**
- mêmes avantages que les membres effectifs + insertion gratuite dans Chimie Nouvelle d'une annonce de demande d'emploi.

Membres résidant à l'étranger
Membres effectifs : **60 euros**
Membres associés : **35 euros**